Aalto University
School of Science
Degree Programme of Computer Science and Engineering

Samuli Vuorinen

Camera Characterization System Calibration and Verification

Master's Thesis
Espoo, April 27th, 2016

Supervisor: Professor Eero Hyvönen
Instructors: Mikko Nuutinen D.Sc. (Tech.), Aalto University
Joni Oja Ph.D., University of Eastern Finland

Aalto University
School of Science
Degree Programme of Computer Science and Engineering

ABSTRACT OF
MASTER'S THESIS

Author: Samuli Vuorinen

Title:
Camera Characterization System Calibration and Verification

Date: April 27th, 2016 **Pages:** 70

Professorship: Media Technology **Code:** T-110

Supervisor: Professor Eero Hyvönen

Instructors: Mikko Nuutinen D.Sc. (Tech.)
Joni Oja Ph.D.

Miniature cameras are common in today's smartphones and other mobile devices. Achieving optimal image quality with such cameras requires elaborate characterization measurements done on the camera in laboratory conditions. The mobile phone company Nokia—and later Microsoft—has built an automated characterization system to perform these measurements.

The quality of the characterization measurements done with this system depends on accurate calibration of the system. Calibration of this system has been tedious manual work, and the process has not been thoroughly documented. The goal of this research was to automate and improve the calibration process using the company's own software platform Mobile Imaging Playground (MIP). The measurement devices were integrated into MIP and all the calibration procedures were implemented as MIP plugins. A high quality spectroradiometer was used as a reference for the calibration. Multiple metrics were explored to evaluate the accuracy of the final system calibration and match to the reference. Uncertainties of the different calibration phases were also analyzed.

For spectrally continuous and relatively smooth illuminants the calibration accuracy was high. Fluorescent spectra with narrow peaks were more problematic. Part of the problem can be attributed to the sparse sampling of the reference device, which causes the fluorescent peaks to be undersampled, so in reality the calibration results are most likely better than this. Keeping this in mind, reproduction of the fluorescent spectra after calibration can be considered at least colorimetrically accurate.

The study proposed some future possibilities to improve the calibration process, for example by using a more suitable reference device and implementing some kind of bandpass correction.

Keywords: Calibration, camera, spectrometer, photonics, uncertainty analysis, light synthesis, metrology.

Language: English

Aalto-yliopisto
Perustieteiden korkeakoulu
Tietotekniikan tutkinto-ohjelma

DIPLOMITYÖN
TIIVISTELMÄ

Tekijä:	Samuli Vuorinen		
Työn nimi:	Kamerankarakterisointijärjestelmän kalibrointi ja verifiointi		
Päiväys:	27. huhtikuuta 2016	**Sivumäärä:**	70
Professuuri:	Mediatekniikka	**Koodi:**	T-110
Valvoja:	Professori Eero Hyvönen		
Ohjaajat:	Tekniikan tohtori Mikko Nuutinen Filosofian tohtori Joni Oja		

Pienoiskamerat ovat yleisiä nykypäivän älypuhelimissa ja muissa mobiililaitteissa. Parhaan mahdollisen kuvanlaadun saavuttaminen näillä kameroilla vaatii tarkkoja karakterisointimittauksia laboratorio-olosuhteissa. Matkapuhelimia valmistava yritys Nokia — ja myöhemmin Microsoft — on rakentanut automatisoidun kamerakarakterisointijärjestelmän näiden mittausten suorittamiseen.

Karakterisointijärjestelmä tuottaa synteettisiä eri valonlähteiden spektrejä. Karakterisointimittausten laatu riippuu järjestelmän eri komponenttien kalibroinnin tarkkuudesta eli tarkkuudesta, jolla järjestelmä kykenee toistamaan ja mittaamaan halutun spektrin. Tämän tutkimuksen lähtökohtana olevan järjestelmän kalibrointi on ollut hidasta käsityötä, ja prosessia ei ole dokumentoitu kovin tarkasti. Tutkimuksen tavoite oli automatisoida ja parantaa kalibrointiprosessia yrityksen omaa ohjelmistoalustaa Mobile Imaging Playgroundia (MIP) käyttäen. Korkealaatuista spektroradiometriä käytettiin referenssilaitteena kalibrointityössä. Lopullisen kalibrointilaadun arvioimiseksi käytettiin useita aiempien tutkimusten perusteella määritettyjä mittoja. Kalibrointivaiheiden epävarmuustekijöiden vaikutuksia ja suuruutta tutkittiin myös.

Spektraalisesti jatkuvien ja verrattain tasaisten valonlähteiden kohdalla lopullisen kalibroinnin tarkkuus osoittautui erittäin hyväksi. Loisteputkivalonlähteet, joiden spektri on piikikäs, toistuivat kalibroinnin jälkeen huonommin kuin jatkuvaspektriset valonlähteet. Tämä johtui luultavasti referenssilaitteen harvasta näytteistyksestä, joka aiheuttaa terävien spektripiikkien alinäytteistymistä. Todellisuudessa loisteputkivalonlähteiden kalibroinnin laatu on siis luultavasti parempi kuin tulokset antavat ymmärtää, ja kalibrointia voidaan pitää kolorimetrisesti tarkkana.

Työssä esitetään myös tulevaisuutta silmällä pitäen muutamia parannusehdotuksia kalibrointiprosessiin, kuten paremman referenssilaitteen valinta ja jonkinlaisen kaistanpäästökorjauksen toteutus.

Asiasanat:	Kalibrointi, kamera, spektrometri, fotoniikka, epävarmuusanalyysi, valosynteesi, metrologia.
Kieli:	Englanti

Acknowledgements

This Master's Thesis was done for the Nokia Camera Image Quality team in Espoo, Finland. I would like to thank the whole team for taking me in and providing me with a great and interesting opportunity to study this topic.

I wish to thank my instructors Mikko Nuutinen (D.Sc.) and Joni Oja (Ph.D.) for their contributions and guidance, and Prof. Eero Hyvönen for supervising this thesis. This thesis would not have been possible without helpful insights from Ari Sirén and the Aalto Visual Media Research Group led by Prof. Pirkko Oittinen.

Further thanks go to Lauri Kangas for advice over the years, and everyone in POLLUX, Kirkkonummen Komeetta ry, Ursa ry and #sirius for helping me pursue my interests in astrophotography.

Last but not least, I extend my biggest thanks to both my family and my lovely partner-in-crime Susanna for supporting me all the way. Thank you for your patience.

Espoo, April 27th, 2016

Samuli Vuorinen

Abbreviations and Acronyms

ADC	Analog-to-Digital Converter
CCD	Charge-Coupled Device
CCT	Correlated Color Temperature
CFA	Color Filter Array
CIE	The International Commission on Illumination (Commission Internationale de l'Éclairage)
CMF	Color Matching Function
CMOS	Complementary Metal Oxide Semiconductor
CRA	Chief Ray Angle
ISO	International Organization for Standardization
IR	Infrared
LED	Light Emitting Diode
MIP	Mobile Imaging Playground
MIPI	Mobile Industry Processor Interface
MOS	Metal Oxide Semiconductor
NIST	National Institute of Science and Technology
SI	The International System of Units (Le Système international d'unités)
SMIA	Standard Mobile Imaging Architecture

Contents

Chapter 1

Introduction

1.1 Background

In the past few years mobile devices, such as smart phones and tablets, have become ubiquitous. Most of these devices sport some type of camera functionality. Thus, digital cameras embedded in mobile devices have become ubiquitous too, they are everywhere! The rise of photocentric social media like Instagram and Flickr has also heightened the importance of cameras to consumers tremendously.

Mobile device manufacturers are very rapidly developing new cameras and introducing new camera modules into commercial products. Camera modules are self-contained modular components that usually include an optical assembly, a digital image sensor and control electronics.

Just reading data off the digital image sensor is not enough to produce a high-quality image. Several characteristics of the camera module need to be determined to correctly process the image data into a final image that corresponds more or less to how a human eye would have seen the scene the camera captured. This process is called called characterization.

Each new camera module requires careful characterization before it can be used in a consumer product. Camera module characterization involves measuring several properties of the camera sensor and optics. To make this process fast and reliable, it has to be ensured that the instruments used in the measurements give correct results as accurately and precisely as possible. This process is called instrument calibration.

Measurements involving light spectra—such as camera characterization—are very sensitive to errors. Small systematic changes in the spectrum of light presented to a camera accumulate over the whole wavelength range, and can cause significant color errors. In addition, small changes in the raw data

extracted from the camera sensor can translate to big changes in the final image due to the image processing algorithms applied by the camera image processing pipeline. Considering these facts, accurate instrument calibration becomes essential to characterize the camera modules properly.

The practical work behind this Master's Thesis was conducted during the years 2013-2015 at Nokia/Microsoft Camera Image Quality Laboratory in Espoo, Finland. The Nokia mobile phone business along with the laboratory was acquired by Microsoft in 2014. The laboratory had a unique combination of measurement devices that enabled highly controllable spectral synthesis, measurement automation and accuracy. The combination of these devices—the camera characterization system—was used to characterize several camera modules used in the Lumia smartphones.

However, calibrating the camera characterization system in question has been tedious manual work, requiring a multitude of very careful measurements under various lighting conditions. Analyzing the measurement results has been done manually, and the process has not been very well documented. Lack of documentation has occasionally delayed necessary calibration work, when the only people knowledgeable of the calibration process have been unavailable.

The calibration process has also been slow and prone to human errors. Calibration from beginning to end has usually taken several days or even a week. Because the calibration process has been so slow, it has often blocked production use of the characterization system. Uncertainties in the calibration have not been determined during the manual calibration process, so the reliability and accuracy of the calibration have been unknown.

1.2 Goals of this thesis

The goal of this thesis is to describe and implement a new, more flexible calibration process for the camera characterization system. The camera characterization system consisted of multiple interlocking instruments and is in production use a large part of the time, so the aim is to calibrate it in a way that requires no disassembly of the system. Sending any part of the system back to the manufacturer or a third party for calibration is costly and slow. Temperature changes and moving the instruments in relation to each other also easily invalidate the calibration. Because of these reasons, the calibration should be done on-site. The calibration process should also be relatively easy and fast, so it would not severely interrupt the production use of the system.

This thesis work had three primary goals, which are listed below:

- Describe and document the camera characterization system components used at the time, and the calibration of the system.
- Specify and implement a calibration system that would make the calibration procedure automatic, and at the same time more reliable and faster.
- Study the results and find metrics to evaluate the performance of the new and improved calibration system and estimate the uncertainty of the resulting data.

This thesis is divided into 9 chapters, starting with this introduction. After chapter 1 the reader should have an understanding of what the target of this thesis is and why was it conducted. Chapter 2 describes the basic concepts of radio- and photometry, which are essential to understanding the measurement instruments and methods used in this thesis. Chapter 3 goes over the basic concepts of colorimetry, such as color-matching functions and color spaces. Chapter 4 introduces the structure of camera devices and the technology used in them to help the reader better understand what kind of devices modern digital camera systems are. Details of the camera characterization process are discussed in chapter 5. The structure and components of the camera characterization system are described and documented in chapter 6. The calibration procedures of the characterization system are shown in chapter 7. The calibration results and conclusions are documented in chapters 8 and 9, respectively.

Chapter 2

Radio- and photometry

2.1 Light

The term "light" usually refers to electromagnetic radiation that is visible to the human eye. Light consists of small quanta of energy called photons. Each photon carries a certain amount of energy with it. Photons exhibit both particle- and wave-like properties. Since photons can be modeled as waves, each photon has a wavelength. The energy of the photon can be described by the equation 2.1, where h is the Planck constant, c the speed of light in vacuum and λ the wavelength of the photon. [1]

$$E = \frac{hc}{\lambda} \tag{2.1}$$

As equation 2.1 shows, the energy of the photon depends only on the wavelength λ of the photon. Eyes can detect electromagnetic radiation of wavelengths between approximately 380 and 780 nanometers. This range is called the visual spectrum of light. [1, 2]

2.2 Radiometry

Radiometry is a field of science that studies the whole spectrum of electromagnetic radiation, ranging from extremely short wavelengths (gamma and X-rays) to very long wavelengths (radio waves). As opposed to photometry, which will be dealt with in detail in section 2.3, radiometry deals with absolute quantities of energy, while photometry takes into account the varying response of the human visual system. [2, 3]

Radiant energy is measured in joules [J] which is a unit derived from the SI base units. Radiant energy is often denoted with the symbol Q. Radiant

energy with respect to time is the radiant power or the radiant flux ϕ, which is measured in watts [W]. The radiant intensity I is then the radiant flux per unit solid angle [$\mathrm{W\,sr^{-1}}$], as described in equation 2.2.

$$I = \frac{\mathrm{d}\phi}{\mathrm{d}\Omega} \tag{2.2}$$

Radiance L is a very fundamental unit in radiometry. Radiance is the radiant power per solid angle per unit projected source area, described in the equation 2.3, where ϕ is the total radiant power, A is the surface area, Ω is the solid angle subtended by the observation and Θ is the angle between the surface normal and the specified direction. Measuring radiance falling on a patch of infinitesimal area dA from direction Ω is illustrated in figure 2.1.

$$L = \frac{\mathrm{d}^2\phi}{\mathrm{d}A\,\cos\Theta\,\mathrm{d}\Omega} \tag{2.3}$$

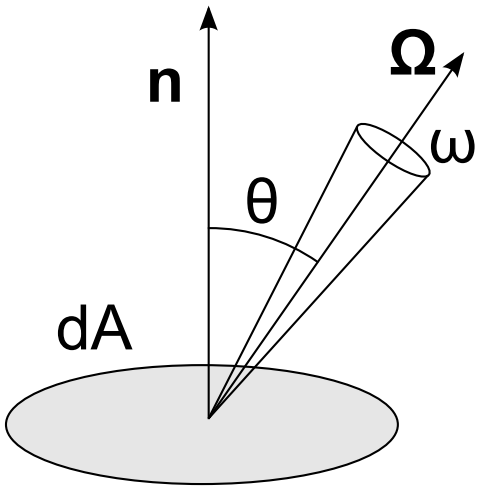

Figure 2.1: Illustration of measuring radiance.

Irradiance E (see equation 2.4) describes the radiant flux per unit area incident on a surface, so the unit of irradiance is $\mathrm{W\,m^{-2}}$.

$$E = \frac{\mathrm{d}\phi}{\mathrm{d}A} \tag{2.4}$$

Irradiance can be calculated by integrating radiance over the the hemisphere visible to the observed point. Radiant exitance is a unit similar to irradiance, but it describes the flux emitted from the surface.

Radiometric units can also be considered as functions of wavelength. For example spectral radiance is simply defined as radiance per wavelength.

$$L = \frac{\mathrm{d}^2\phi}{\mathrm{d}A\,\cos\Theta\,\mathrm{d}\Omega\,\mathrm{d}\lambda} \tag{2.5}$$

As can be seen from equation 2.5, the unit of spectral radiance is $\mathrm{W\,sr^{-1}\,m^{-3}}$. Spectral radiance can also be considered as a function of frequency [Hz] instead of wavelength [m].

2.3 Photometry

Photometry is very similar to radiometry described in section 2.2, but photometry only examines the visible wavelenghts of electromagnetic radiation, and takes into account the spectral response of the human visual system by weighting spectra with the so called spectral luminous efficiency function $V(\lambda)$. [4]

The two main spectral luminous efficiency functions are the photopic and scotopic luminosity function, which correspond to the sensitivity of the cone and rod cells in the human eye respectively. The sensitivity of the human eye in most normal lighting conditions is mediated by the cone cells, while the rod cells remain saturated. In this kind of lighting the sensitivity of the eye corresponds well to the photopic luminosity function, which peaks at the wavelength of 555 nanometers. A graph of the photopic luminosity function is shown in figure 2.2. [1]

In very low lighting conditions the rod cells start to respond and the peak spectral sensitivity of the eye shifts approximately 50 nanometers towards shorter wavelengths, corresponding to the scotopic function. In intermediate lighting a third function is sometimes also used, called the mesopic luminosity function. [1]

Radiometric quantities can be converted to the corresponding photometric quantities by using the spectral luminous efficiency function as a spectral weighting function, as in equation 2.6, where ϕ_v and ϕ are the corresponding photometric and radiometric quantities, λ is the wavelength of light and V is the photopic luminosity function. The result of the integration can be

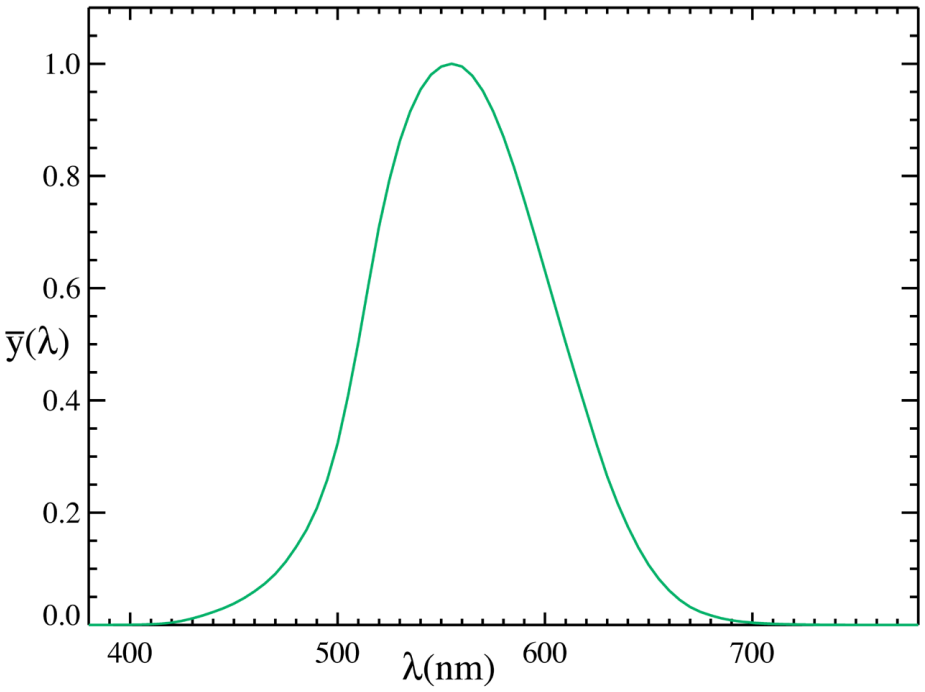

Figure 2.2: Graph of the photopic luminosity function.

multiplied by the constant $K_m = 683\,\mathrm{lm/W}$ to obtain photometric units at an absolute scale. [1, 2]

$$\phi_v = K_m \int_{380}^{780} \phi(\lambda)\, V(\lambda)\, \mathrm{d}\lambda \tag{2.6}$$

Calculating a photometric quantity for a single wavelength λ_0 reduces simply to equation 2.7.

$$\phi_v(\lambda_0) = K_m\, \phi(\lambda_0)\, V(\lambda_0) \tag{2.7}$$

The very basic photometric quantity is the luminous flux ϕ_v, expressed in lumens [lm], which is completely analogous to the radiometric unit of the radiant flux ϕ. The radiant flux is just weighted with the spectral luminous efficiency function to get the luminous flux.

Luminous intensity I_v is similarly analogous to the radiometric quantity radiant intensity I. Luminous intensity is expressed in candelas [cd] which equals lumens per unit solid angle [lm/sr]. The photometric equivalent of radiance L is luminance L_v, and can be expressed as luminous intensity per unit projected area [$\mathrm{cd\,m^{-2}}$]. Finally, illuminance E_v is similar to the

radiometric quantity irradiance E, and is measured in luxes [lx] or lumens per unit area [$\mathrm{lm\,m^{-2}}$]. Illuminances in common lighting conditions are listed in table 2.1.

The corresponding radiometric and photometric quantities are summarized in the table 2.2.

Table 2.1: Examples of illuminances in common lighting conditions.

Lighting conditions	Illuminance
Sunny day	100 000 lx
Overcast day	1 000 lx
Office lighting	500 lx
Home lighting	100 lx
Full moon at night	0.1 lx

Table 2.2: Corresponding radiometric and photometric quantities.

Radiometry	Photometry
Radiant energy [J]	Luminous energy [lm s]
Radiant flux [W]	Luminous flux [lm]
Irradiance [$\mathrm{W\,m^{-2}}$]	Illuminance [lx]
Radiant intensity [$\mathrm{W\,sr^{-1}}$]	Luminous intensity [cd]
Radiance [$\mathrm{W\,sr^{-1}\,m^{-2}}$]	Luminance [$\mathrm{cd\,m^{-2}}$]

Chapter 3

Colorimetry

Colorimetry is the branch of science that studies and describes human color perception. Even though camera characterization does not directly involve human color perception, colorimetry introduces some useful concepts, such as *tristimulus values*, *metamerism* and *color spaces*. Light as such has no color, only some wavelength. A perception of color occurs when light hits the human eye and causes a response in the visual system. [1]

The retina of a human eye has two kinds of photoreceptor cells: rods and cones. Rods are only active in very low lighting conditions, while cones are used in brighter lighting. Cone cells are divided into three subtypes, whose spectral sensitivies peak at different wavelengths, thus enabling the resolution of different wavelengths into different colors. Because of the three types of cone cells, the human color vision is said to be trichromatic. Since there are only one type of rod cells, color vision is not possible in extremely low light. [1, 5]

The three cone cell types are classified as sensitive to long, medium and short wavelengths of light, and are often abbreviated as L, M and S cones. Figure 3.1 shows the normalized cone cell sensitivities. [1, 5]

The photopic and scotopic luminosity functions described in section 2.3 correspond to the total sensitivity of cone and rod cells, respectively. [1]

Describing colors in terms of the fundamental cone responses would be a very straightforward approach, but the cone responses have been succesfully determined only recently, so other means have been developed. So called color-matching functions (CMF) have been empirically determined to map light spectra into three-dimensional coordinates called *tristimulus values*. [1, 4]

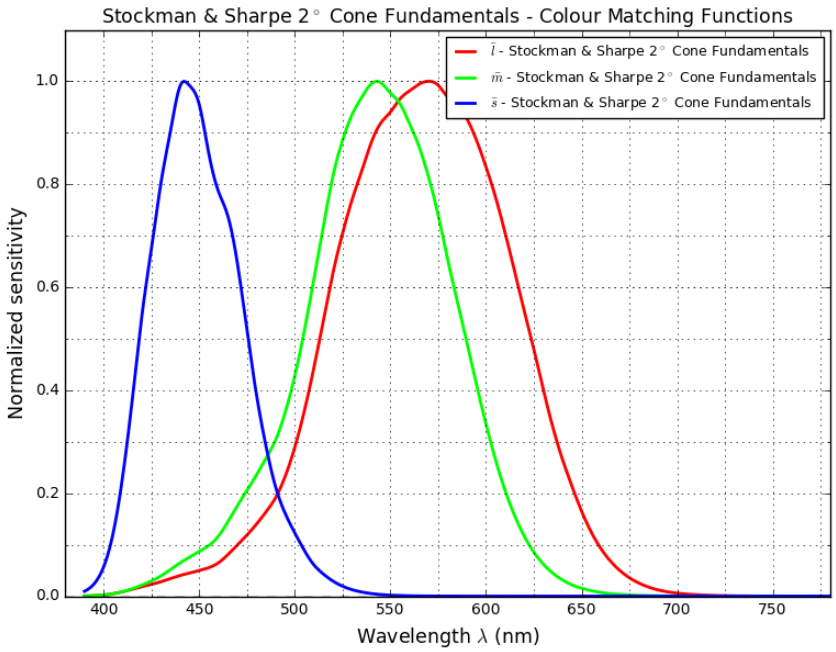

Figure 3.1: Cone cell sensitivities, by Stockman and Sharpe [5].

3.1 Color-matching functions

In the 1920s and 1930s Wright [6] and Guild [7] were the first to determine the correspondence between different monochromatic lights and three adjustable light sources called primaries. In their experiments, test subjects tried to match a color produced by a monochromatic light source by adjusting the relative amounts of the primaries. Based on the data gathered on the relative amounts of the primaries for each monochromatic light source Wright and Guild were able to form color-matching functions for mapping spectra to three tristimulus values.

Later The International Commission on Illumination (CIE) transformed the data so that it corresponds to monochromatic primaries at 435.8 nm, 546.1 nm and 700.0 nm, and standardized the CMFs. By integrating the observed light spectrum weighted by the color matching functions over the visible wavelength range — as shown in equations 3.1—the tristimulus values are obtained. **R**, **G** and **B** are the CIE RGB tristimulus values, ϕ is the observed light spectrum and $\bar{r}$, $\bar{g}$ and $\bar{b}$ are the CIE RGB color-matching functions. [1, 4]

$$\mathbf{R} = \int_{\lambda} \phi(\lambda) \cdot \bar{r}(\lambda) d\lambda \tag{3.1a}$$

$$\mathbf{G} = \int_{\lambda} \phi(\lambda) \cdot \bar{g}(\lambda) d\lambda \tag{3.1b}$$

$$\mathbf{B} = \int_{\lambda} \phi(\lambda) \cdot \bar{b}(\lambda) d\lambda \tag{3.1c}$$

The tristimulus values identify the color of the measured light. If the tristimulus values of two different spectra match, they are perceived as the same color. [1, 4]

CIE also devised an improved set of CMFs—$\bar{x}$, $\bar{y}$ and $\bar{z}$—where the CMF values are always positive, and $\bar{y}$ corresponds to the standard photopic luminance response function CIE $V(\lambda)$. This set of CMFs is known as the CIE 1931 standard observer. The tristimulus are calculated exactly as the CIE RGB values in equation 3.1, except the CIE RGB color-matching functions are replaced with $\bar{x}$, $\bar{y}$ and $\bar{z}$. The CMFs are visualized in figure 3.2. [1, 4]

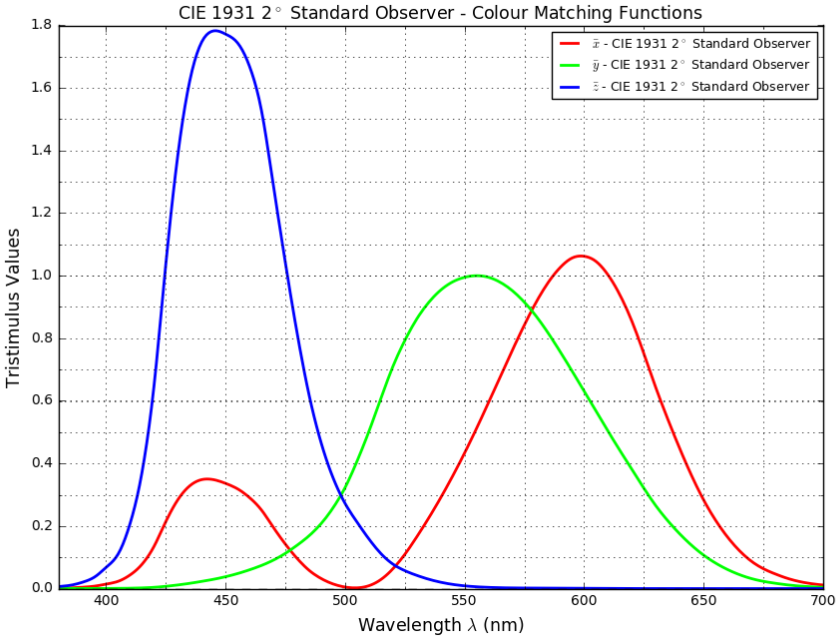

Figure 3.2: CIE 1931 standard observer color-matching functions.

Because of the trichromatic nature of human color vision, it is possible to construct multiple significantly different spectral power distributions, that

cause the same response in the visual system, i.e. are seen as the same color. This also means that they have the same tristimulus values. This phenomenon is called *metamerism*. [1, 4]

3.2 Color spaces

As shown earlier, the human visual system is trichromatic, so any perceived color can be represented as a vector of three numbers, or tristimulus values. Different CMFs and tristimulus values form color spaces. The tristimulus values derived from spectral power distributions by integrating with the CMFs $\bar{x}$, $\bar{y}$ and $\bar{z}$ form the standard CIE XYZ color space. [1]

CIE XYZ is able to represent all possible colors, but in practice the color space might not be suitable for all purposes. It might be necessary to use a color space that enables efficient encoding and transmission of data. Another common reason for using some other color space is that it provides better perceptual uniformity. Simple Euclidean distance in CIE XYZ does not correspond to perceptual difference in color. Color difference metrics are described in more detail in section 3.3. [1]

The CMF primaries define the boundaries of each color space. The range of colors the color space is able to represent is called the *gamut*. [1, 4]

CIE XYZ is often used as a device-independent method for representing colors, but is usually transformed to some other color space for storage or display. sRGB is one of the most common color spaces in use today. CIE XYZ is also often used as an intermediate color space for transforming from one color space to another, since most color spaces are defined relative to CIE XYZ. [1]

3.3 Color difference metrics

Encoding colors as tristimulus values enable quantifying differences between colors. Most color spaces are not perceptually uniform, so a simple Euclidean distance measure in e.g. CIE XYZ does not give a meaningful metric for comparing colors. CIELAB and CIELUV color spaces are color opponent spaces standardized by CIE, and include a non-linear compression to achieve better perceptual uniformity. CIELAB consists of the tristimulus values L^*, a^* and b^*. One commonly used color difference metric is CIELAB ΔE^*_{ab}, which is the Euclidean distance in CIELAB space, shown in equation 3.2. [1]

$$\Delta E^*_{ab} = [(\Delta L^*)^2 + (\Delta a^*)^2 + (\Delta b^*)^2]^{1/2} \tag{3.2}$$

ΔE^*_{ab} was designed to quantify small color differences in laboratory conditions, and it does not extend well to large color differences. More accurate color difference metrics are CMC, CIE 1994 and CIEDE2000. [1]

Chapter 4

Camera technology

4.1 Camera structure

The basic structure of camera devices has stayed the same nearly throughout the whole history of photography. Camera devices consists of an optical assembly or a pinhole and some sort of a medium to capture the image projected by the optics.

For a very long time the dominant medium was photographic film. However, in the past few decades digital image sensors have taken over the field of photography. Modern image sensors are described in section 4.2, and section 4.3 deals with the basics of optical systems. Issues specific to small sensors, such as the camera sensors found in mobile devices, are described in section 4.4.

The characterization system described in chapter 6 deals with optical spectrometers. Optical spectrometers are technologically very similar to digital cameras systems, so their relationship is probed more closely in section 4.5.

4.2 Image sensor technology

Modern digital image sensors designed for the visual wavelengths of light are based on semiconductor technology. Digital image sensors consist of photodetector arrays, which convert incident photons to electric charges.

The light sensitivity of semiconductor photodetectors is based on the generation of electron-hole pairs in the semiconductor, when photons hit the photodetector material [2]. The photodetector structure is designed to prevent the electron-hole pairs from recombining, so the number of generated charges can be measured.

The two predominant types of digital image sensors are so called CCD and CMOS sensors. The main difference between the two types is how the electric signals are transferred off the sensor and amplified for subsequent processing. The image sensor types are examined in more detail in section 4.2.3. [2, 8]

The most common photodetector types are MOS capacitors and photodiodes. According to many literary sources MOS capacitors are used in CCD sensors and photodiodes in CMOS sensors, but in reality they are often used somewhat interchangeably [2]. The photodetector types are examined in more detail in sections 4.2.1 and 4.2.2.

4.2.1 MOS capacitors

MOS (metal oxide semiconductor) capacitors are one of the two predominant photodetector types used in digital image sensors. Metal oxide semiconductor refers to the structure of the capacitor, which consists of a *metal* contact called the gate, a thin *oxide* layer and a P-type *semiconductor* (usually doped silicon). The structure is illustrated in figure 4.1. [2]

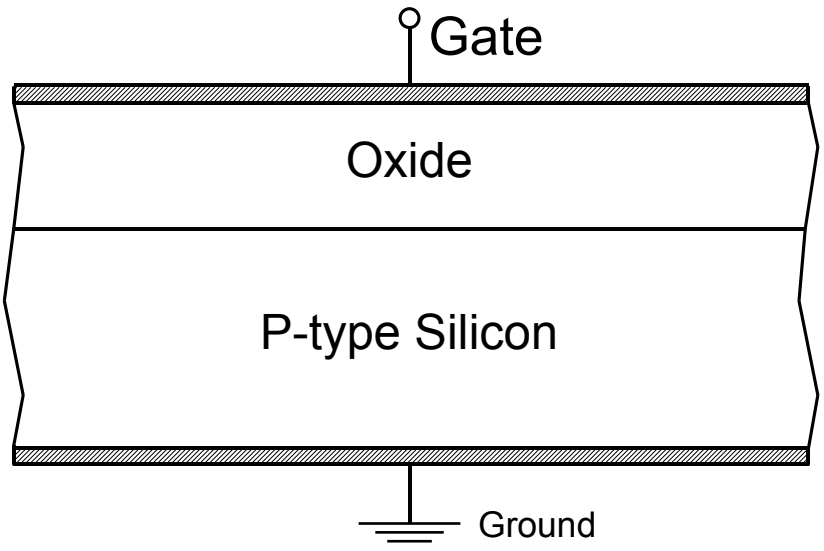

Figure 4.1: The structure of a MOS capacitor. Adapted from an illustration by Cyril Buttay. [9]

When incident photons hit the semiconductor, they generate electron-hole pairs in the material. To prevent the pair from instantly recombining, a constant positive bias voltage is applied to the gate, while the semiconductor is grounded. This configuration causes the negatively charged electrons to gather at the interface between the semiconductor and the oxide layer, while holes move in the opposite direction. [2]

4.2.2 Photodiodes

All semiconductor components react to incident light by generating charge carriers. Since this is usually an unwanted effect, the components are packaged inside a light blocking casing. Photodiodes are fundamentally ordinary semiconductor diodes which have not been packaged, thus permitting photons to penetrate the material. [2]

Diodes and photodiodes alike consist of a junction of a P-type and N-type semiconductor, or a PN-junction. A depletion region is formed at the interface of the two semicondutor types. When an incident photon hits the depletion region, the different charge carriers migrate in opposite directions without the need for a constant bias voltage. [2]

The sensitivity and the full well capacity of the photodiode can be increased by adding a layer of intrisic semiconductor material in the middle of the PN-junction, resulting in a so called PIN-junction. This kind of photodiodes are often called pinned photodiodes, and are very widely used in image sensors. [2]

4.2.3 CCD and CMOS

One of the two most common image sensor types employ charge-coupling for transferring the accumulated charges from the image sensor pixels to the signal processing chain outside the sensor. This kind of image sensors are commonly called CCD image sensors. [2, 8, 10]

Charge-coupling refers to a technique for storing and transferring charge packets in a semiconductor device. Devices which utilize this technique are called Charge-Coupled Devices (CCD). In image sensors charge-coupling works by sequentially transferring the contents of each pixel towards one specified edge and reading out the contents of that edge column. The charges can be transferred from one pixel to the next by applying a certain voltage sequence to the pixel gate contacts. [10]

CCD image sensor are often described as passive pixel sensors, as the signal amplification and analog-to-digital conversion happens outside the pixels. Contrary to CCD, most CMOS image sensors place the amplifier and

analog-to-digital converter (ADC) inside each single pixel. This kind of a sensor architecture is called an active pixel sensor.

Complementary Metal Oxide Semiconductor (CMOS) refers to technology used to fabricate integrated circuits, but in a camera device context CMOS has become synonymous with active pixel sensors constructed with CMOS technology. [2, 8].

4.2.4 Microlenses

The topmost layer of modern image sensors often consists of an array of very small lenses called microlenses, illustrated in figure 4.2. The light sensitive photodetector does not usually cover the entire pixel, so a part of the pixel is not sensitive to light at all. To alleviate this problem, microlenses are used to focus the incident light on to the light sensitive area of the pixel. In the figure these light sensitive areas are shown in light gray, while other areas are shown in dark gray. The color filters under the microlens array are part of the color filter array, which is described in more detail in section 4.2.5.

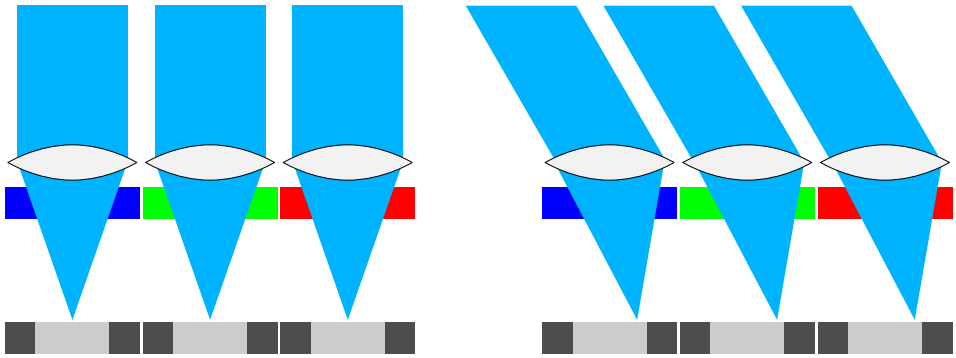

Figure 4.2: Illustration of microlenses on image sensors. The light gray rectangles represent the photosensitive areas of the pixel.

Microlenses are extremely important to the light sensitivity of modern image sensors. Depending on the device, they can increase the effective pixel fill factor by 30-70 % [2]. With the exception of telecentric lenses, the chief ray angle (CRA) of the incident light varies with position on the sensor. If the CRA becomes too large, the microlenses might accidentally focus light on an adjacent pixel, causing optical crosstalk between the pixels. This issue is discussed in more detail in section 4.4.2. To mitigate this kind of problems the individual positions of the microlenses can be optimized for specific fields

of view so the microlenses are offset from the pixel centers on the edges of the sensor [2].

4.2.5 Color imaging

Digital image sensors are inherently monochromatic in the sense that they cannot distinguish colors, but only intensities of light. The sensitivity of the sensor varies according to the wavelength of light, but once a photon has been converted to electric charges in the sensor, there is no way of reconstructing the wavelength of the original photon.

Several methods for capturing color images are in use. The three most common ways of recording color images with a digital image sensor are described below.

A very simple solution is a device called a filter wheel or a filter slider. The device contains a holder for several color filters, and mechanically rotates or slides the holder to place different filters in front of the sensor, like in figure 4.3. Usually the device is placed between the image sensor and optics, or in some rare cases in front of the optical assembly. Full color images can be formed by combining several images captured with different color filters. Because the images are not captured simultaneously, color images of moving objects are difficult to achieve using filter wheels or sliders. Mechanical filter changers are also very big and bulky, and they contain moving parts. This makes them unfeasible for mobile applications. However, filter wheels and sliders are widely used in scientific applications, especially in astronomy.

A more advanced method of acquiring color images is splitting the incoming beams of light into components using a color separation prism, filtering each component with a different color filter and directing them to separate image sensors, as seen in figure 4.4. F_1 and F_2 represent different filter coatings, which reflect blue light and red light respectively, and transmit other wavelengths. This method has the advantage of being able to capture all the needed images simultaneously, but requires the use of several image sensors instead of one. Also, color separation prisms are quite large and thus are difficult to use with mobile camera devices.

The only currently feasible solution for mobile color imaging is the usage of a so called color filter array (CFA). The CFA is an array of color filters placed directly on top of the image sensor, like in figure 4.5. Each pixel receives only a portion of the visible spectrum, and the missing components are reconstructed based on the surrounding pixels. This procedure is often called demosaicking or debayering. Because of the filter array, all the color channels are subsampled, which results in reduced optical resolution. [13]

Very often the CFA consists of repeating blocks of 4x4 pixels with red,

Figure 4.3: A partially disassembled QSI 583 astronomical CCD camera with an integrated filterwheel. Photograph by QSI Press Photos. [11]

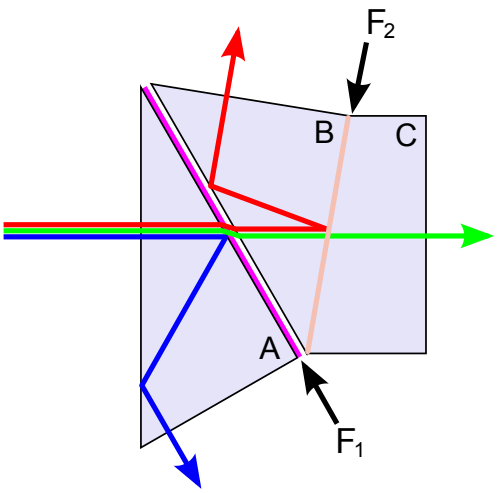

Figure 4.4: A trichroic prism splitting the light spectrum into three parts. Illustration by Colin M. L. Burnett. [12]

green and blue primary color filters [8]. Currently the most common filter pattern in consumer camera sensors is the so called Bayer matrix pattern [13],

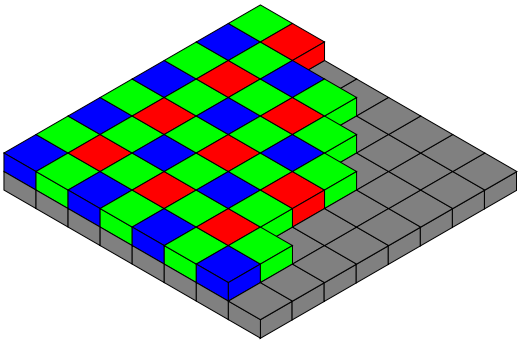

Figure 4.5: Color filter array on an image sensor. Illustration by Colin M. L. Burnett. [14]

which contains twice as many green filters as blue or red filters. However, some manufacturers, like Kodak [15] and Fujifilm [16], have experimented with more exotic filter combinations and patterns. Foveon has developed a filterless sensor, which separates colors based on how far into the sensor silicon the photons penetrate, since the depth varies significantly with the light wavelength [17].

4.3 Optics

To capture images, a digital camera needs some kind of a mechanism to form an image of the outside world on to the image sensor. Perhaps the simplest mechanism consists of a very small aperture, called a pinhole. The working principle of a pinhole is illustrated in figure 4.6.

Since the pinhole aperture by definition is very small, the light gathering power is weak. The small aperture also results in poor optical resolution because of diffraction effects.

Most modern camera systems employ various optical lens assemblies to form the image on the image sensor. This has the benefit of greatly increasing the light gathering aperture and optical resolution.

Real life optical systems usually consist of multiple lenses, but the fundamentals of geometric optics can be illustrated with a single lens, with spherical optical surfaces. For simplicity's sake the lens can initially be considered a thin lens, meaning it has infinitely small thickness.

Figure 4.7 shows such thin lens focusing paraxial (parallel to the optical axis L) light rays to a single point at a distance of f (the focal length) from the lens. This point is called the focal point. The focal length of a thin lens

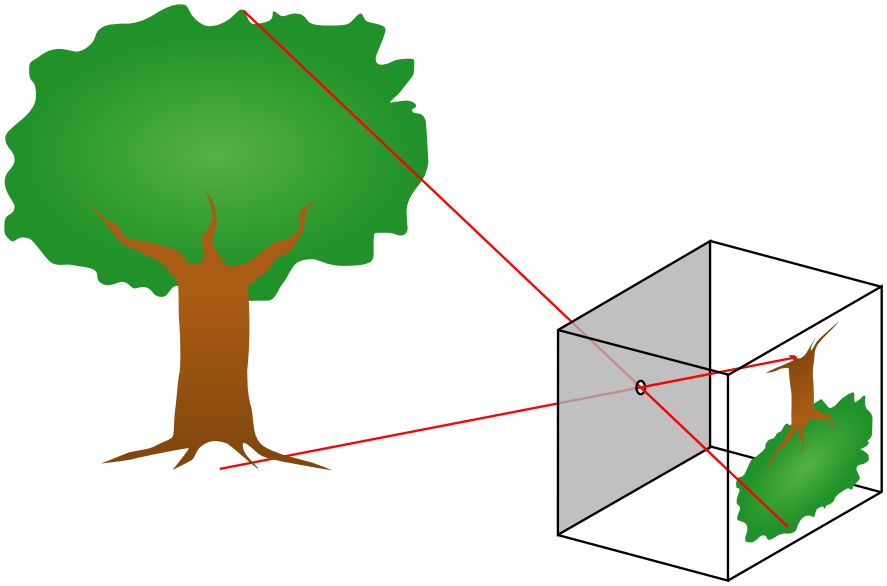

Figure 4.6: The pinhole camera principle.

can be calculated using the equation 4.1 if the index of refraction n of the lens and the radii of curvature R_1 and R_2 of the lens sides are known.

$$\frac{1}{f} = (n-1) \cdot (\frac{1}{R_1} - \frac{1}{R_2}) \tag{4.1}$$

In real life lenses have a finite thickness. The same expression for a lens with thickness d is shown in equation 4.2.

$$\frac{1}{f} = \frac{n-1}{R_1} + \frac{1-n}{R_2} + \frac{d(n-1)^2}{nR_1R_2} \tag{4.2}$$

The light gathering power of a lens system can be described with the so called F-number (F), which is defined in equation 4.3 [8], where θ is half of the opening angle of the focused light rays in figure 4.7. The bigger the F-number is, the less light hits the image sensor per unit area.

$$F = \frac{1}{2\sin\theta} \tag{4.3}$$

As a result of the equation, the theoretical minimum for the F-number is 0.5. When θ is small, the distance from the focal point to the edge of the lens

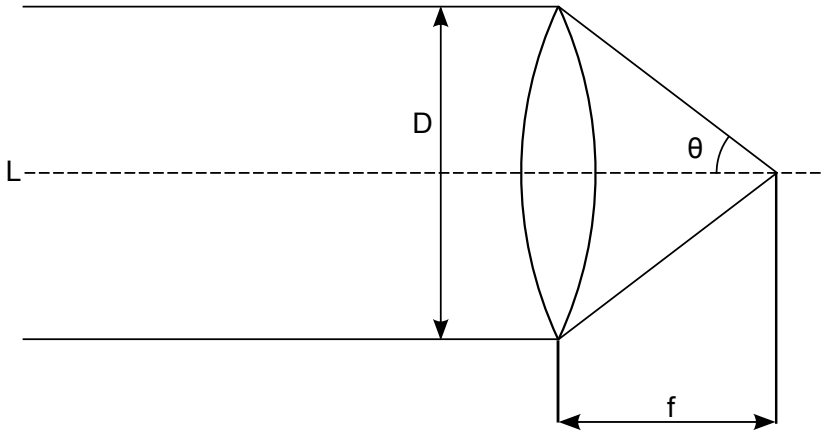

Figure 4.7: Diagram of a single thin lens with the focal length f and the aperture diameter D.

is nearly equal to the focal length, and equation 4.3 can be approximated with equation 4.4.

$$F = \frac{f}{D} \tag{4.4}$$

Optical elements absorb part of the incoming light, but the transmissivity can be enhanced with the use of coatings [8]. The F-number does not take into account the light absorption or other transmission losses.

Due to the wave-like nature of light, the image of a perfect point light source formed by aberration-free optics is not a perfect point, but a small disk surrounded by dim rings, as illustrated in figure 4.8. This pattern is called the Airy disk. The angular size of this pattern depends on the aperture of the optics and the light wavelength. The physical size r of the pattern on the sensor can be approximated from the F-number of the optics by equation 4.5, where λ is the wavelength and F the F-number. [1, 8]

$$r = 1.22\lambda F \tag{4.5}$$

r in equation 4.5 is also called the *Rayleigh limit*, and it indicates the

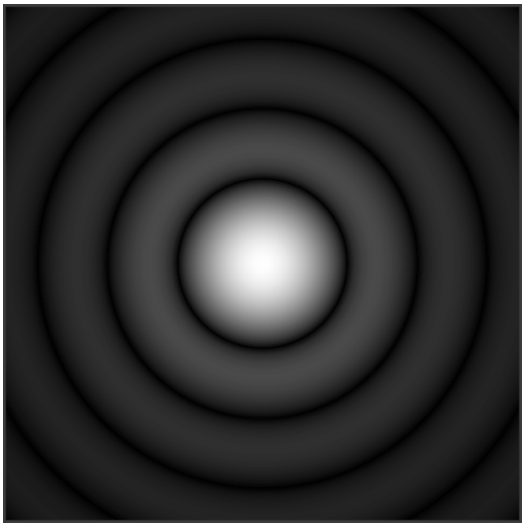

Figure 4.8: Plot of the Airy disk pattern.

minimum spacing between two infinitesimally small points that can just be distinguished optically. Rayleigh chose the first dark ring of the Airy disk as the criterion of resolving power for a two-point image. [1, 8]

4.4 Mobile camera module specific issues

Because the characterization system under consideration is aimed towards mobile camera devices, some mobile camera module specific issues have to be considered. The key difference between mobile and other camera devices is the camera module size, which sets constraints on module design.

4.4.1 Physical pixel size

Mobile devices usually employ very small image sensors. Combined with the need for high resolution images, the physical size of individual pixels becomes very small.

Since the readout electronics on each pixel require some space, the pixel fill factor decreases with pixel size. This can be alleviated to some extent by placing microlenses on each sensor pixel. Also, the smaller physical size directly means that less photons hit the pixel per unit time, resulting in lower signal-to-noise ratio, so the sensitivity obviously decreases with pixel size. [1, 8]

The maximum amount of unit charges a pixel can store is mostly dependent on the physical size of the pixel. The smaller pixels get, the less charges they can store. This means that small pixels have less dynamic range than big pixels. Dynamic range in this context refers to the range of scene brightness levels that can be captured in the same image by the camera sensor. [1]

4.4.2 Color shading

Small camera modules aimed towards mobile devices are prone to so called color shading, which means that the color reproduction properties of the image sensor vary spatially. Silicon-based image sensors are sensitive to infrared radiation, which is usually blocked using an IR cutoff filter. [1]

The most common IR cutoff filters are based on thin-film interferential filters, whose spectral transmissivity changes as a function of the angle of the incident light. Because the mobile camera modules use wide-angle lenses and the lens assembly is placed very close to the sensor, the incident light angle at the edges of the sensor is very steep. This causes the sensor's effective spectral response to be different in the edges and the center of the sensor. [18]

4.4.3 Green imbalance

Image sensors with physically very small pixels are prone to problems with so called green imbalance.

As described in section 4.2.5, image sensors in mobile devices have a color filter array laid on top of the image sensor. The most common color filter array pattern contains twice as many green filters as there are red or blue filters. Usually the filters repeat in groups of 4 pixels, where on one row there is a red and a green filter, and on another row there is a green and a blue filter. Often in small image sensors the effective spectral response of the two green filters in each group are systematically different. This is called green imbalance. [19]

The main reasons for this are both optical and electrical crosstalk between adjacent pixels. Bigger pixels are more immune to crosstalk because of the more complex structure and longer distance between individual pixels, and smaller chief ray angles in most bigger cameras. [20–22]

As mentioned in section 4.2.4, optical crosstalk happens when microlenses accidentally focus light into adjacent pixels. This usually happens with big chief ray angles, or in other words near the edges of the sensor. Electrical crosstalk is often attributed to minority carrier diffusion from pixels to

adjacent pixels. [20]

4.5 Relationship to optical spectrometers

There are several sorts of spectrometer designs operating in the visible wavelength range of light, but in this thesis we will focus on spatially dispersive spectrometers, since all the spectrometer devices described in chapter 6 are based on this technique. A spectrometer combines a light collection system, a spectrograph and an optoelectronic detection and processing system to estimate the power spectral density of the incident light. A spectrograph is defined as a device that physically isolates spectral channels using optical elements. [23]

Spatially dispersive digital spectrometers are technologically very similar to digital cameras. The simplified basic structure of a 4F spectrometer described by James [23] is shown in figure 4.9, where F is the focal length of the lenses.

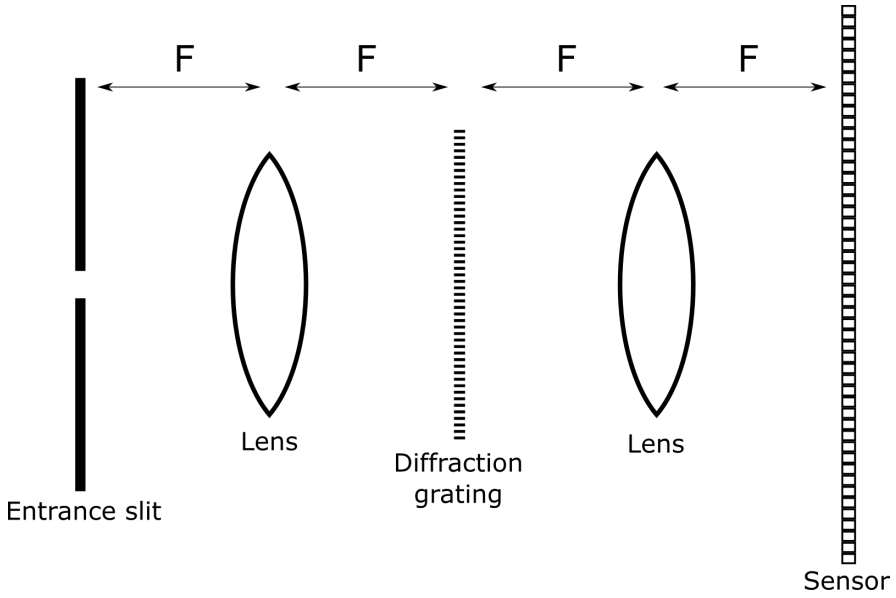

Figure 4.9: Simplified structure of a 4F spectrometer.

The incoming light is guided through a narrow slit, and an image of the slit is projected onto a grating or through a prism. The grating or prism disperses the incoming light into a spectrum, and an image of the spectrum is captured using a photodetector array, such as a CCD or CMOS sensor described in section 4.2. The spectral resolution of the spectrometer

is inversely proportional to the width of the entrance slit, but making the slit narrower lets less light in. This way the slit width is always a compromise between resolution and signal-to-noise ratio. [23, 24]

Chapter 5

Camera characterization

Digital cameras record irradiance values of the scene projected onto the image sensor via an optical assembly. Different irradiance values at different wavelengths of light produce different responses on the sensor, which the camera encodes as digital values. Camera optics, all the filters between the scene and the sensor, the sensor itself and the camera software all distort the recorded signal in some way or another. Reinhard et al. [1] define camera characterization as the process of recovering the relationship between these scene irradiance values and the pixel encoding produced by the camera.

Reinhard et al. [1] also describe two general approaches for camera characterization. The first approach is based on measuring the response of the camera to different wavelengths of light. Calculating the mapping from scene irradiances to camera responses becomes trivial once the spectral sensitivity of the camera is known. This method requires specialized equipment, but the measurement process is relatively fast and can be automated. The camera spectral sensitivity is described in more detail in section 5.3.

The second approach relies on physical color calibration targets. Several standard color samples are measured under constant illumination using a spectrophotometer, and images of the color samples are captured using the camera under characterization. A very common color calibration target *GretagMacbeth ColorChecker* is shown in figure 5.1. With enough color samples and multiple illuminants, a thorough mapping from CIE XYZ values to camera RGB values can be formulated. This method is relatively inexpensive, but requires manual labor and the potential accuracy is not as good as with the first approach. It is also worth noting that methods following this second approach are not able to characterize any spatial variation in the spectral sensitivity of the camera, unlike methods following the first approach. [1, 25]

The camera characterization system described in chapter 6 is capable of measuring the spectral sensitivity of a camera directly, so only the first

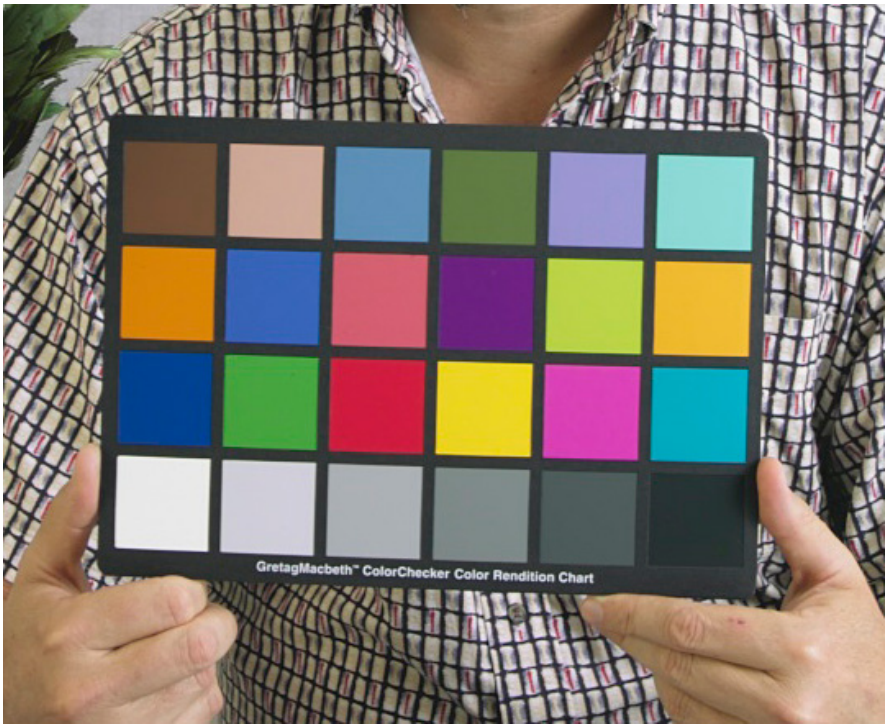

Figure 5.1: *GretagMacbeth ColorChecker* color calibration target. Photograph by Richard F. Lyon. [26]

approach of the two is covered in this thesis.

The following sections describe the essential attributes of a camera that have to be determined to succesfully characterize a camera. The central attributes are as follows:

- *Pedestal signal of the camera*, i.e. the output signal level when there is no input signal.
- *Linearity/non-linearity* of the output signal relative to the input signal.
- *Spatial spectral sensitivity* of the camera sensor.

The characterization system under calibration in this thesis can automatically measure these attributes.

5.1 Pedestal

When no light hits the camera sensor, the sensor still produces some non-zero output signal. Let us call this signal the pedestal signal in this thesis. This

signal comprises of two main components: *bias* and *dark current*. [1, 10, 27]

Bias is a constant offset in the output signal, and it originates from the detector and amplifier electronics of the sensor. The bias signal of a single pixel does not variate per se, but the electronics add some random variation to the output called *readout noise*. [10, 27]

The dark current is an integration time dependent and temperature dependent signal produced by lattice defects in the silicon detector. In the absence of incident photons, thermal agitation of the silicon sensor slowly releases free electrons in the detector, which add to the output signal. Since the release of each electron is a statistically independent event, the noise inherent in the dark current signal obeys Poisson statistics. Thus a dark current signal of x electrons will have a statistical uncertainty of $\sqrt{x}$ electrons. At any given temperature, the rate of dark current electrons freed is constant, but the rate approximately doubles for each 6 degrees Celsius that the temperature rises. [1, 27]

Figure 5.2 shows the pedestal level and the input photon signal as a function of time. The output signal level at any time t is the sum of the photon signal, dark current signal and bias level at that time t. Any changes in temperature would affect the slope of the dark current signal in the graph.

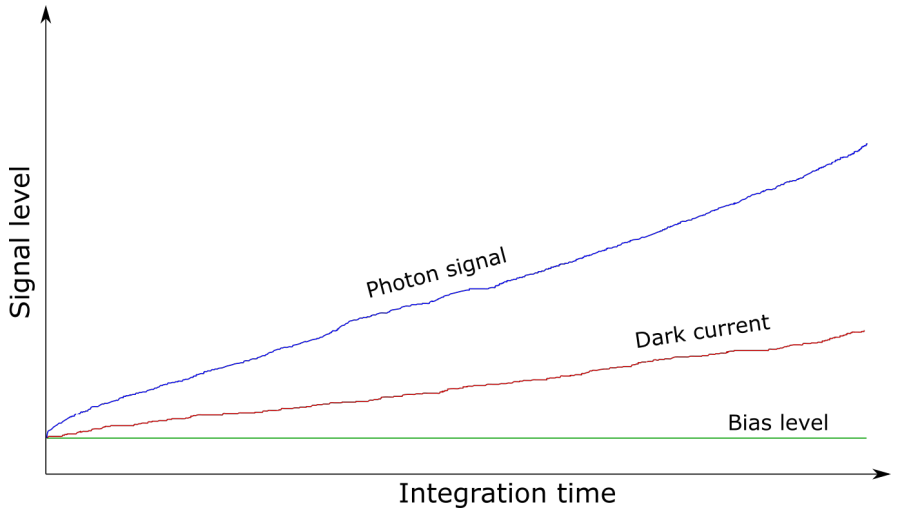

Figure 5.2: Example pedestal and input signal levels as a function of time.

The pedestal signal, in general, is not uniform over the whole camera sensor. Both bias and dark current can variate from pixel to pixel due to manufacturing processes and defects. This spatial variation is called Fixed-Pattern Noise or FPN, and is often divided into two components: *Dark Signal Non-Uniformity (DSNU)* and *Photo-Response Non-Uniformity (PRNU)*. Re-

gardless of the name, DSNU is used to describe both dark signal and bias signal non-uniformity. PRNU referes to pixel-to-pixel differences in photodetector sensitivity or amplifier gain. [1, 10, 27]

In the ideal case the pedestal signal for each pixel is considered and modeled separately, but usually some compromises have to be made due to data storage or processing power restrictions. Berry and Burnell [27] suggest measuring the pedestal level by covering the camera to prevent light from hitting the sensor and exposing images with multiple exposure times, temperatures and gain levels. Refining the captured data to a spatial model of the camera pedestal signal depends heavily on the use case, and is outside the scope of this thesis. Once the pedestal signal is known, it can be subtracted from the camera output signal to determine the real input signal (the photon signal).

5.2 Linearity

An ideal camera sensor would always exhibit an output signal that is linearly proportional to the input. Simply put, when the intensity of light seen by the camera changes by a factor of x, the pixel values of the raw image should change by a factor of nx, where n is a positive constant. Most digital camera sensors are fairly linear, but to achieve a high degree of accuracy in color reproduction, the camera response has to be characterized, and any nonlinearities corrected. [28]

There are multiple ways of determining the linearity of a camera's intensity response. Vora et al. [29] propose a method where images are captured under multiple intensities of light, and the intensity is simultaneously measured using a photometer. The same could be achieved without the photometer by varying exposure times instead of adjusting the light source, given that the exposure time control is reliable and accurate, and the light source stable. Bérube et al. [28] measured the linearity of a camera by capturing an image with multiple reflectance calibration targets under even illumination. Once the measurements are done, the camera response can be compared to the known intensities, and corrected accordingly.

5.3 Spectral sensitivity

Light sensitivity of a camera sensor varies by wavelength. The natural sensitivity of silicon is modified by any filters or coatings on the sensor and optics. In the common case of an RGB color camera, the pixels are divided into three groups: red, green and blue, as explained in section 4.2.5. When the spectral

sensitivity of each pixel group is known, it is possible to calculate the camera response of an arbitrary spectrum without the need of synthesizing the spectrum in real life and capturing an image of it using the camera under characterization.

Measuring the spectral sensitivity requires specialized equipment. Reinhard et al. [1] suggest using a radiance meter and a monochromator to measure the spectral sensitivity. A monochromator is a device that is capable of emitting light at a single user-specified wavelength at a time. The programmable light source that is part of the system under calibration (see section 6.1.1) in this thesis is capable of acting as a monochromator, in addition to producing any other arbitrary spectrum.

Using these devices it is possible to step through the whole wavelength range of visible light, showing the camera only one wavelength of light at a time and simultaneously measuring the monochromator intensity with the radiance meter. Using the data captured using both the camera and a radiance meter, a very accurate model of the camera spectral sensitivity can be produced. [1]

Since the camera characterization system under calibration in this thesis is built to characterize very small camera modules for smartphones and other mobile devices, special attention must be paid to mobile camera specific problems described in section 4.4. All cameras and optical assemblies suffer from vignetting (also called shading). With most cameras this only affects the amount of light reaching the sensor, but not the spectral power distribution. This is called luminance shading. For very small camera modules with steep chief ray angles vignetting also changes the spectral sensitivity of the sensor. An example of this spatial variation in spectral sensitivity is shown in figure 5.3. The phenomenon is called color shading. [18]

Traditionally luminance and color shading has been characterized by capturing images of uniformly illuminated test charts or the inside of an integrating sphere under various illuminants. These are called flat field images. Figure 5.4 shows an example of a flat field image. The effects of color shading are clearly visible as color non-uniformity over the image. Since the majority of color shading is caused by bandpass shift of the infrared cutoff filter as a function of incidence angle, color shading is very dependent on the spectrum of the illuminant [18]. If an illuminant carries no power in the wavelengths where the infrared cutoff filter bandpass variates, color shading will not be visible under that particular illuminant. In practice, flat field images for all common light sources have to be captured to correct color shading in all normal circumstances.

This problem can be sidestepped by measuring the spectral sensitivity of the camera spatially, i.e. as a function of location on the sensor. Im-

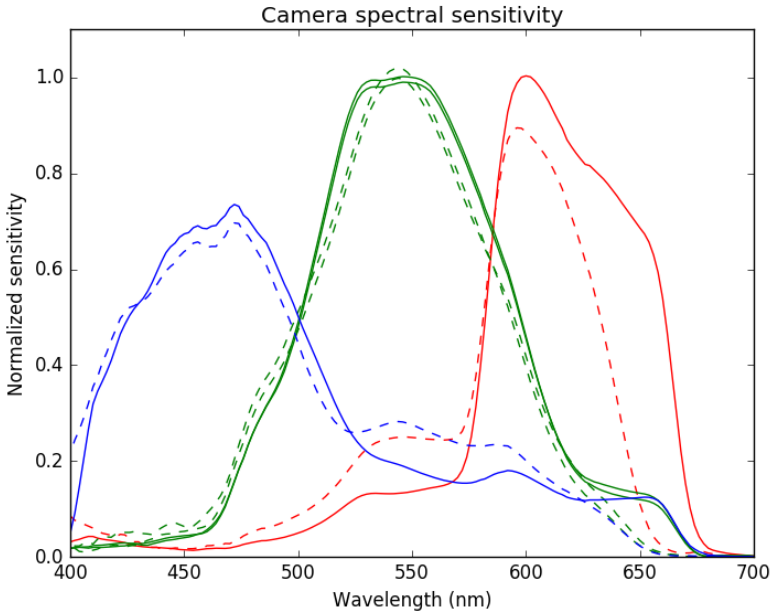

Figure 5.3: Example of a typical mobile camera module spectral sensitivity. Solid lines show the sensitivity measured at the center of the sensor, and dashed lines show the sensitivity measured near one corner of the sensor. The colors of the lines correspond to red, green and blue filters of the color filter array on the sensor.

ages equivalent of flat field images under any spectrum can be synthesized when the spectral sensitivity is known. Due to fabrication defects and sensor microlens variation the spectral sensitivity can significantly vary even pixel-to-pixel, and this can be diagnosed and corrected if the spectral sensitivity is known spatially. [1]

Figure 5.4: Example image of camera color shading. Photograph from I3A CPIQ White Paper. [18]

Chapter 6

Characterization system

This chapter describes the camera characterization system under calibration and documents the components used to build it. The structure of the characterization system is fairly simple. The system consists of a programmable light source connected to an integrating sphere, a spectrometer measuring the light from the integrating sphere, and a camera platform. The devices are controlled with an ordinary personal computer. The system is visualised in figure 6.1.

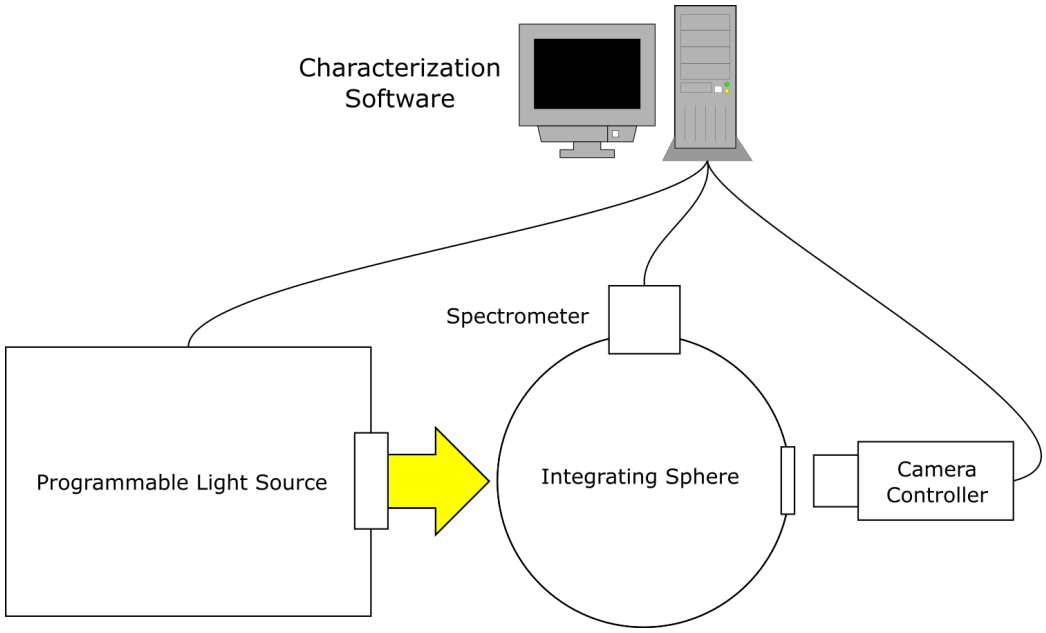

Figure 6.1: Structure of the characterization system.

The light source controlled by the PC produces the synthetic light spec-

trums needed for characterization work, and feeds them to the integrating sphere. Both the camera platform and the spectrometer look inside the integrating sphere. By using a feedback loop with the spectrometer and the light source it is possible to achieve the wanted spectrum very precisely. This, however, requires careful calibration of the spectrometer used. Details of the calibration work are shown in chapter 7. After the correct spectrum has been achieved, the computer controlled camera platform captures the necessary characterization images.

6.1 Available devices

This section describes all the different devices used to build the camera characterization system.

6.1.1 Programmable light source

The Googh & Housego OL 490 Agile Light Source [30, 31] is a programmable light source, powered by a xenon arc lamp and a Digital Micromirror Device (DMD) used to synthesize any light spectrum within the bounds of the xenon arc lamp spectrum [32]. The OL490 connected to a xenon lamp and a power source is pictured in figure 6.2.

Figure 6.2: The Gooch & Housego OL490 Agile Light Source. Image by Gooch & Housego. [30]

The DMD consists of an array of MEMS-controlled micromirrors [32]. The incoming light passes through a diffraction grating, which disperses the

light into separate wavelengths. The dispersed spectrum lands on the micromirror array and can then be selectively dimmed by controlling the angle of the micromirrors. [31]

6.1.2 Spectrometers

The characterization system itself contains only one spectrometer (Ocean Optics USB2000+), but the reference spectrometer used for calibration (Photo Research PR-650) is also documented here.

The Ocean Optics USB2000+ Miniature Fiber Optic Spectrometer is a compact, general-purpose spectrometer. The device is shown in figure 6.3. It is used to actively monitor the light source output in the characterization system. The device includes built-in EEPROM memory bank for calibration data. The calibration data includes stray light compensation, wavelength calibration and linearity calibration coefficients. See chapter 7 for more details about device calibration. [33]

Figure 6.3: Ocean Optics USB2000+ miniature spectrometer. Image by Ocean Optics Inc. [33]

The PR-650 SpectraScan Colorimeter in figure 6.4 is a portable spot spectroradiometer by Photo Research Inc. The spectrometer sensor is a 128

pixel linear CCD detector. The device output ranges from 380 nm to 780 nm at a 4 nm resolution. The measuring field of the device is 1°. [34]

Figure 6.4: The Photo Research PR-650 SpectraScan Colorimeter. Image by The Photo Research Inc. [34]

The PR-650 spectrometer was used as a calibration reference for the rest of the devices. However, the calibration system software supports using an arbitrary spectrometer as a reference device, as long as it can be controlled using Mobile Imaging Playground software environment. The control software and Mobile Imaging Playground are described in detail in sections 7.6 and 7.6.1 respectively.

6.1.3 Integrating sphere

An 8.2" Gigahertz-Optik UM integrating sphere [35] is connected to the programmable light source to provide a very uniform light intensity for the whole field of view of the camera module.

6.1.4 Camera control

The camera modules are controlled with a Scooby2 Platform [36] by ATRA Vision Inc. Scooby2 is a modular platform designed for controlling MIPI and SMIA compatible camera modules over an IEEE1394 FireWire connection. Mobile Industry Processor Interface (MIPI) and Standard Mobile Imaging Architecture (SMIA) are sets of standard specifications defining various as-

pects of how to communicate with mobile camera modules [37, 38]. The Scooby2 platform is pictured in figure 6.5.

Figure 6.5: The ATRA Vision Inc. Scooby2 Platform. Image by the ATRA Vision Inc. [36]

6.1.5 Characterization software

The control software for the camera characterization system runs on an ordinary Windows PC. The software automatizes the image capturing part of the characterization process described in chapter 5, and is also able to do a few other proprietary measurements developed at Nokia/Microsoft. Further details of the software are out of the scope of this thesis.

Chapter 7

System calibration

When the camera characterization system is under calibration, the camera platform is replaced with a reference spectrometer. Otherwise the characterization system is kept intact. A diagram of the calibration setup is shown in figure 7.1.

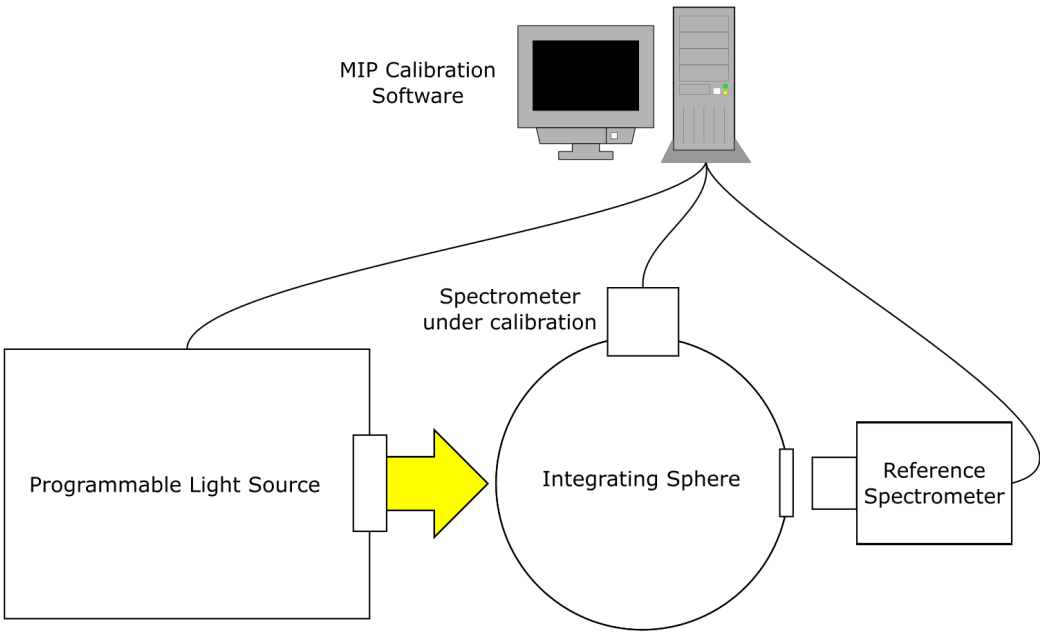

Figure 7.1: Structure of the calibration setup.

Since the programmable light source spectrum is iteratively corrected based on the feedback received from the spectrometer, the accuracy of the system is only dependent on the accuracy of the used spectrometer. Sensors

on most modern spectrometers are based on the same CCD/CMOS technology as digital cameras, so calibrating a spectrometer is very similar to characterizing a camera.

Zwinkels [39] suggests the following calibration steps for a spectoradiometer:

- Pedestal calibration
- Wavelength calibration
- Spectral intensity calibration

Linearity of the device response must also be verified and possibly corrected. All the other calibration phases assume linearity of the data. [39]

Before proceeding with the calibration, it must be ensured that the instrument to be calibrated is stable. Perhaps the most common reason for instability is the changing temperature of the measurement device or the reference target [39].

7.1 Traceability

The calibration of the characterization system components must be traceable to well known calibration standards. This means that it should be possible to relate the result of measurement to a (national or international) calibration standard through an unbroken chain of comparisons. An estimate of calibration uncertainty should also be included in the trace.

In the case of this thesis, the reference device Photo Research PR-650 [34] is used as a reference standard, and Photo Research guarantees that their devices are traceable to calibration targets or devices used by the National Institute of Science and Technology (NIST), called NIST calibration standards. Photo Research reports an estimated uncertainty of $\pm 2\%$ for spectral measurements with their devices [40].

7.2 Pedestal calibration

Pedestal level (also called zero error by Zwinkels [39]) refers to the signal produced by the measurement device when there is no input signal. This case is identical to the pedestal level of a camera, as described in section 5.1. In the case of a spectroradiometer the input signal is the amount of light hitting the sensor. If the pedestal level is temporally stable, it can simply be measured and subtracted from the actual measurement data. [39]

The pedestal level of a spectroradiometer can be measured by preventing any incident light from reaching the sensor, and by recording the output signal of the device. The pedestal of a digital spectoradiometer consists of the inherent bias level of the sensor and the dark current signal accumulated over the integration time. Because of the dark current signal, the pedestal level is dependent on the length of the integration time. [1, 10]

The pedestal level of the instrument under calibration—Ocean Optics USB2000+—varies with temperature, but the instrument does not contain a temperature regulation system, so creating a pedestal model as a function of wavelength, integration time and temperature is difficult. For the characterization system, the problem has so far been solved by repeatedly measuring the pedestal right before each actual measurement. The programmable light source has a physical shutter which can be used to block any light from entering the integrating sphere during the pedestal level measurement. An average of these pedestal level measurements can then be subtracted from the actual measurements to get rid of the cumulative error introduced by the pedestal in the spectrum.

7.3 Linearity calibration

Accuracy of spectral measurements requires that the output signal of the detector is linearly proportional to the input signal. Often this is not the case in real life, so the nonlinearity has to be measured and compensated by calibration if necessary. Linearity of the sensor can be determined by measuring a stable light source with varying integration times. The sensor response should be linearly proportional to the integration time.

The device under calibration—USB2000+—has built-in linearity correction, which is implemented as a 7th degree polynomial correction function. The corrected output O is calculated by dividing the input signal I with the correction function f_c, as shown in equation 7.1. [41]

$$O = \frac{I}{f_c(I)} \tag{7.1}$$

The correction function can be thought of as the relative sensor response as the function of the input signal level. In the ideal case the sensor response to a certain light flux does not depend on the current input signal level, so in that case the correction function $f_c = 1$. In real life the sensor response is usually lower near the extremes of the sensor dynamic range, i.e. when the sensor element is nearly empty of charges or nearly full. Examples of a perfect response and a normal response are shown in figure 7.2.

The polynomial correction coefficients are stored in the device memory. The built-in correction assumes that the linearity does not vary as a function of wavelength, so the device provides the same linearity correction for all wavelengths. [41]

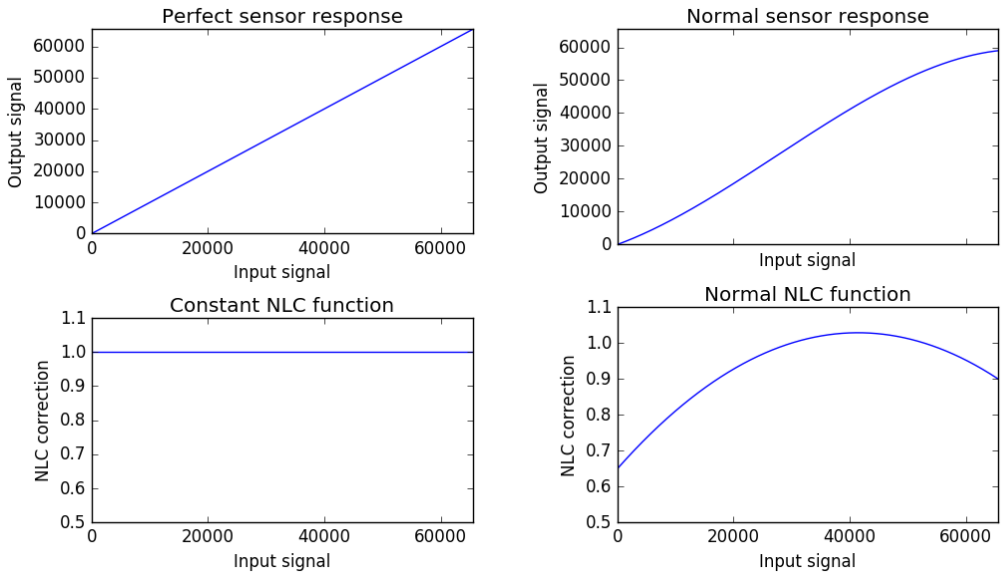

(a) Perfectly linear sensor response.

(b) Normal sensor response.

Figure 7.2: Example sensor responses and their corresponding non-linearity correction (NLC) functions.

7.4 Wavelength calibration

Wavelength calibration is done to ensure that the spectrometer output wavelengths actually correspond to the actual wavelengths of the measured light. The wavelength accuracy can be verified by taking spectral measurements of light sources with very accurately known spectral peaks. The wavelengths of the known peaks can then be compared with the spectrometer output, and used to correct for any deficiencies.

Several commercial light sources for wavelength are available, such as the Optronic Laboratories OL 700-24 Wavelength Calibration Source [42]. However, to keep the characterization system setup intact during the calibration procedure, the programmable light source was used to synthesize a suitable calibration spectrum. Since the wavelength range of the instrument is calibrated to match the reference device, the exact calibration spectrum does

not matter. A very accurately known and stable calibration light source is only needed when the calibration is done without any reference devices.

The calibration spectrum was synthesized so that it contained a narrow peaks with 10 nanometer spacing. This resulted in 19 peaks in the range visible to the PR-650 spectroradiometer. USB2000+ raw measurement data of the wavelength calibration spectrum is shown in figure 7.3.

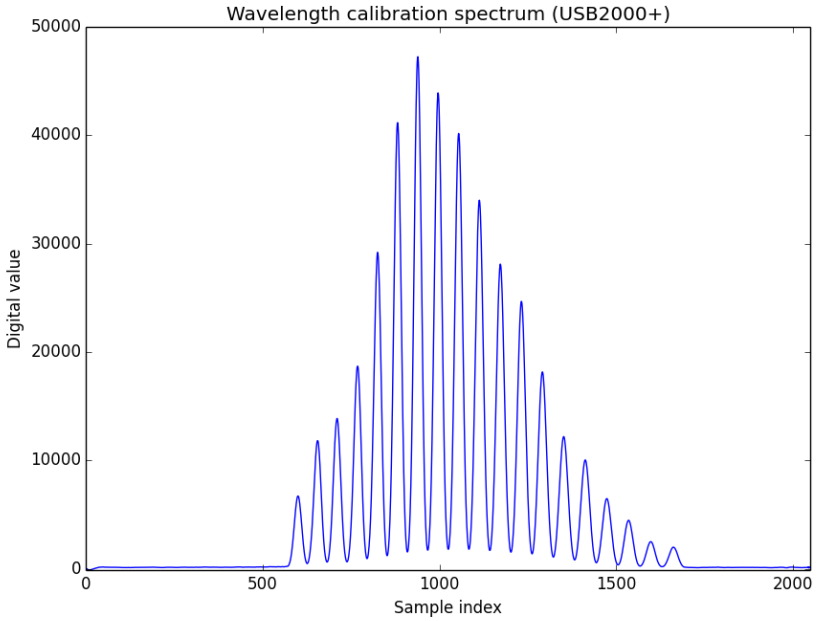

Figure 7.3: The wavelength calibration spectrum synthesized with the programmable light source and measured with USB2000+.

The USB2000+ spectoradiometer contains built-in wavelength calibration system and memory for the calibration data. Each pixel in the linear CCD sensor of the device corresponds to some specific wavelength. The device uses a third-order polynomial to convert raw digital values to actual wavelengths. The calibration polynomial is shown in equation 7.2, where the λ_p is the calibrated wavelength for each pixel p on the spectroradiometer CCD sensor. I is the intercept of the polynomial, which translates to the wavelength of the first pixel, whose index p is 0. C_n are the calibration coefficients. [41]

$$\lambda_p = I + C_1\, p + C_2\, p^2 + C_3\, p^3 \tag{7.2}$$

Figure 7.4 shows the effects of the different calibration coefficients to the resulting spectrum. If $\lambda_p = p$, the assigned wavelength for each pixel of the

sensor would be the index of the pixel, meaning that the first pixel ($p = 0$) would correspond to the wavelength of 0 nanometers, the second pixel to 1 nanometers and so forth. In the second plot the wavelengths are offset by I and scaled by C_1 to roughly match the wavelengths of the reference device and the device under calibration. In the two subsequent plots the terms $C_2\,p^2$ and $C_3\,p^3$ are added to accurately map the pixel indices to real wavelengths.

Due to the fairly sparse 4 nm spectral resolution of PR-650 and the narrow spectral peaks in the calibration spectrum, just choosing the local maxima is not enough to determine the peak locations accurately. The peaks are located by first finding the 19 brightest local maxima in the spectrum, and then fitting second-degree polynomials to the neighbourhoods of the maxima. The peaks of the polynomial curves provide fairly accurate estimates of the spectral peak locations. To lessen the impact of noise on peak finding the spectrum is smoothed with an average filter before peak finding.

Based on the measured peak locations for both the device under calibration and the reference device, the wavelength calibration polynomial can be fit to the data using least squares regression.

7.5 Spectral intensity calibration

The purpose of spectral calibration is to establish a relative spectral response of the instrument under calibration. The spectral response can be achieved by measuring a known light source with the device and adjusting the device output based on the known spectrum. [43]

Measuring a known calibration spectrum $S_{cal}(\lambda)$ using an uncalibrated instrument with an unknown spectral response of $R(\lambda)$ results in an uncalibrated output of $O_{cal}(\lambda)$, as seen in equation 7.3, where λ represents the wavelength of light. It is assumed that the pedestal level of the device is subtracted from the output of the device under calibration, and the wavelength calibration is done.

$$O_{cal}(\lambda) = S_{cal}(\lambda) \times R(\lambda) \tag{7.3}$$

The wavelength-dependent calibration coefficients $C(\lambda)$ can be obtained by dividing the known calibration spectrum $S_{cal}(\lambda)$ with the uncalibrated output data $O_{cal}(\lambda)$, as presented in equation 7.4. The calibration coefficients are device-specific.

$$C(\lambda) = \frac{S_{cal}(\lambda)}{O_{cal}(\lambda)} \tag{7.4}$$

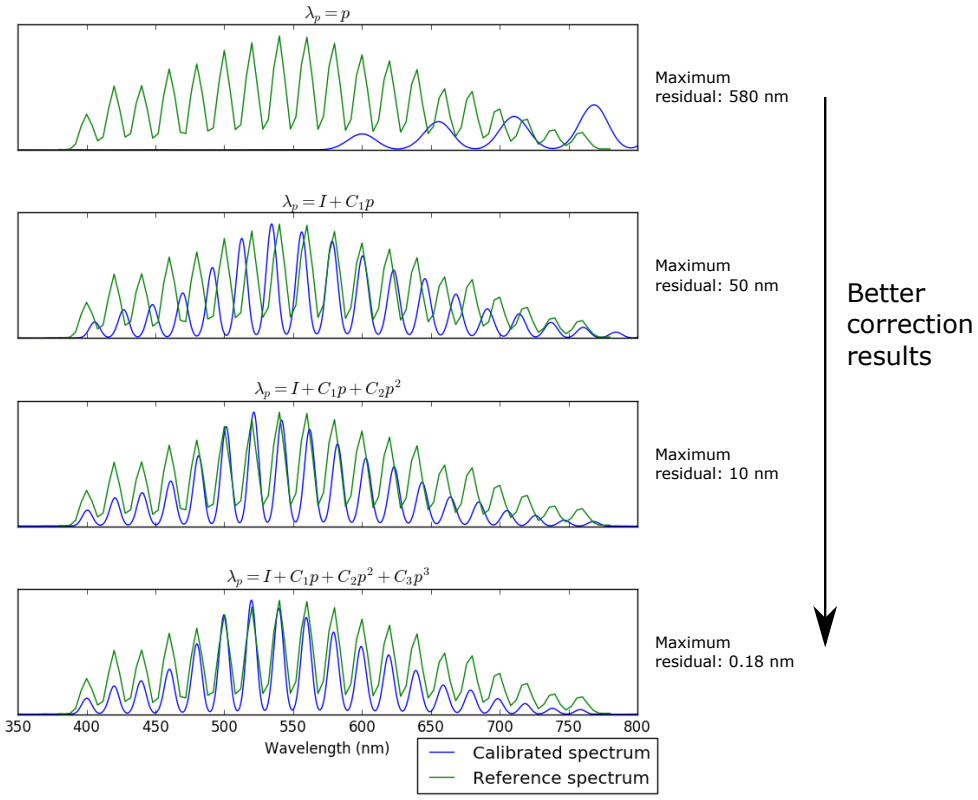

Figure 7.4: Visualization of the effects of the different wavelength calibration coefficients to the end result.

Once the calibration coefficients $C(\lambda)$ have been derived from the spectral response $R(\lambda)$, the coefficients can be used to calibrate raw output data $O(\lambda)$ obtained in equation 7.5.

$$O(\lambda) = U(\lambda) \times R(\lambda) \tag{7.5}$$

The unknown spectrum $U(\lambda)$ is extracted by multiplying the output data with the calibration coefficients $C(\lambda)$ as in equation 7.6.

$$U(\lambda) = O(\lambda) \times C(\lambda) \tag{7.6}$$

To achieve sufficient signal-to-noise ratio in the spectral measurements, the integration time I_O of the spectroradiometer is varied. To make the calibration coefficients independent of integration time the raw spectral output of the device under calibration must be normalized by dividing the signal with the exposure time.

When the integration time I_O is taken into account, the equation 7.4 takes the form of equation 7.7. The final calibrated spectrum $U(\lambda)$ is calculated then as shown in equation 7.8.

$$C_{norm}(\lambda) = \frac{S_{cal}(\lambda)}{\frac{O_{cal}(\lambda)}{I_O}} = \frac{I_O\, S_{cal}(\lambda)}{O_{cal}(\lambda)} \tag{7.7}$$

$$U(\lambda) = \frac{O(\lambda) \times C_{norm}(\lambda)}{I_O} \tag{7.8}$$

In reality the device output for each wavelength is affected by spectral contents of the neighbouring wavelengths because of finite optical resolution. Compensating for this is called bandpass correction. There are multiple methods for bandpass correction [44–46], but they are computationally very expensive and are prone to introducing false artefacts into the corrected spectrum. They are also complex to implement. Because of these downsides, they are not dealt with in this thesis. To simplify calculations, it is assumed that the spectral intensity calibration coefficients for each wavelength are independent of their neighbours.

7.6 Software

The calibration system control software was developed on top of *Mobile Imaging Playground* (MIP), a testing and visualization platform for image and video processing algorithms developed by Nokia. The Scooby2 Platform was already supported by MIP, but the light source and spectrometer controls

had to be implemented separately as MIP plugins. MIP is described in detail in section 7.6.1. The software system built in this Master's Thesis is described in 7.6.2.

Many of the available devices had some sort of support for the Microsoft .NET framework [47], which led to the use of the framework and the programming language C# [48] developed by Microsoft specifically for the .NET environment. MIP is also implemented with C# and .NET.

7.6.1 Mobile Imaging Playground

Mobile Imaging Playground (MIP) is a Nokia-based testing/development platform for image and video processing algorithms, developed by Jeremias Raime, Aleksi Knuutila and Bartek Pawlik. MIP is developed completely in C# and the Microsoft .NET environment. Because MIP facilitates making custom modules for the software, controlling any kind of devices via MIP is very easy.

On a concept level, MIP is very similar to National Instruments LabVIEW [49] and MathWorks Simulink [50], providing a graphical "playground" and numerous intercompatible modules, which the user can drag and drop to easily build a custom system to achieve a specific goal. These arrangements of MIP modules and their connections can then be saved as playground files. The graphical user interface of MIP is shown in figure 7.5.

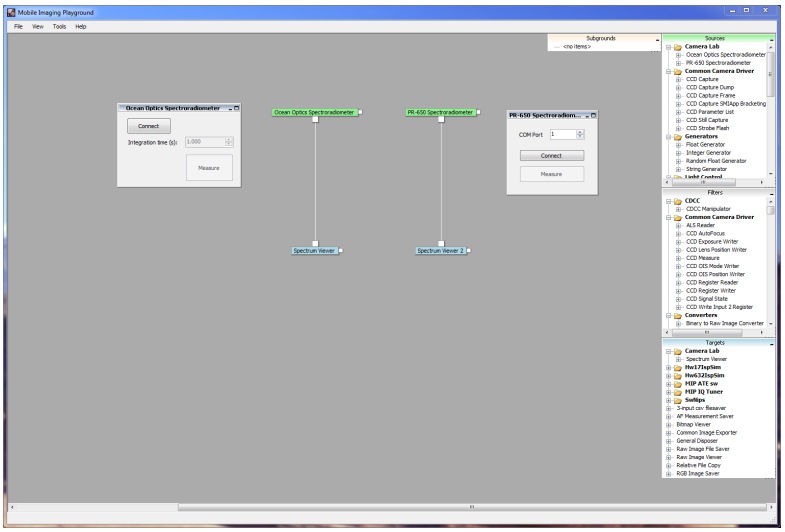

Figure 7.5: The Mobile Imaging Playground graphical user interface.

Most of the user interface is occupied by the playground, where the user

can drag and drop MIP modules and draw connections between module inputs and outputs. All available modules are categorized and listed on the right edge of the user interface.

All MIP modules can have both inputs and outputs, which they use to receive and send data from module to module. MIP modules are divided into three groups based on the number of inputs and outputs. *Source* modules have one or more output, but no inputs. *Target* modules only have inputs, but no outputs. *Filter* modules have both inputs and outputs. The different module types are listed in table 7.1.

Table 7.1: Summary of MIP module types.

MIP Module type	Inputs	Outputs
Source	No	Yes
Filter	Yes	Yes
Target	Yes	No

7.6.2 Calibration system software

The whole calibration system was implemented as collection of MIP plugin modules. Each device is represented by a separate plugin, as are different calibration calculations. The modularity of MIP makes extending the system and reusing any components later very easy. Both spectrometers and light sources implement shared interfaces, so individual devices can be changed without affecting the rest of the system.

Different phases of the calibration process were implemented as individual playgrounds in MIP.

Chapter 8

Verifying calibration results

This chapter presents the results of the automated calibration process with estimated uncertainties. Section 8.1 introduces several metrics that can be used to estimate differences between spectra, in this case the device under calibration and the reference device. The actual calibration data is presented in section 8.2. Finally in section 8.3 the accuracy of the calibration method is evaluated using the metrics presented in section 8.1.

8.1 Spectral difference metrics

There are multiple metrics in use to evaluate differences or similarities between spectral measurements. In this section the following metrics are described:

- Root mean square error (RMSE) and its variants [51, 52]
- Goodness-of-fit coefficient (GFC) [51, 53]
- Euclidean distance (ED) [54]
- Spectral Angle Mapper (SAM) [54]

All the described methods assume identical sampling for both spectra being compared. For equations 8.1–8.6 S_1 and S_2 are the spectra under comparison, and λ is the wavelength.

Root mean square error (RMSE) is a statistical metric used to evaluate the difference of two discretely sampled signals. RMSE is very easy to calculate and simple to understand, but there are no hard rules on what constitutes an acceptable difference and what does not. Equation 8.1 shows

how RMSE is calculated. RMSE is in same units as S_1 and S_2. The smaller the RMSE values are, the better the match between the two spectra.

$$\mathrm{RMSE} = \sqrt{\frac{\sum_\lambda (S_1(\lambda) - S_2(\lambda))^2}{n}} \tag{8.1}$$

RMSE can be converted to relative units by normalization. The two most common ways to do this are called *Normalized Root Mean Square Error* or NRMSE, and Coefficient of Variation of the RMSE or $\mathrm{CV_{RMSE}}$. The definitions of RMSE and $\mathrm{CV_{RMSE}}$ are shown in equations 8.2 and 8.3, respectively. $\bar{S_1}$ in equation 8.3 refers to the mean value of S_1.

$$\mathrm{NMRSE} = \frac{\mathrm{RMSE}}{\max(S_1) - \min(S_1)} \tag{8.2}$$

$$\mathrm{CV_{RMSE}} = \frac{\mathrm{RMSE}}{\bar{S_1}} \tag{8.3}$$

Goodness-of-fit coefficient (GFC) is a metric proposed by Romero et al. [53]. GFC is described in equation 8.4. GFC values range from 0 to 1, where 1 indicates a perfect match. Romero et al. [53] found that GFC ≥ 0.995 means the spectral match is colorimetrically accurate and when GFC ≥ 0.999 the match can be considered very good. For GFC ≥ 0.9999 the match is excellent.

$$\mathrm{GFC} = \frac{\left|\sum_\lambda S_1(\lambda)\, S_2(\lambda)\right|}{\sqrt{\left|\sum_\lambda S_1(\lambda)^2\right|}\,\sqrt{\left|\sum_\lambda S_2(\lambda)^2\right|}} \tag{8.4}$$

Euclidean distance (ED) is a simple straight-line distance between vectors $\mathbf{S_1}$ and $\mathbf{S_2}$, which are formed from the spectral radiance samples of S_1 and S_2. ED is described formally in equation 8.5. The smaller the Euclidean Distance between the two vectors is, the better the match.

$$\mathrm{ED} = \|\mathbf{S_1} - \mathbf{S_2}\| = \sqrt{\sum_\lambda (S_1(\lambda) - S_2(\lambda))^2} \tag{8.5}$$

The usefulness of ED depends on the situation. If the shape of the spectral power distribution of the spectra is identical, but the absolute radiance is different, ED will have large values. ED can be used if the absolute value of the spectra is important.

Spectral Angle Mapper (SAM) addresses some of ED's shortcomings by only comparing the angle between vectors $\mathbf{S_1}$ and $\mathbf{S_2}$, so scaling the absolute radiance of the spectra does not affect SAM, if the spectral power distribution shape stays the same. SAM is defined in equation 8.6. The smaller the angle

between the two spectrum vectors is, the better the shapes of the spectra match.

$$\text{SAM} = \arccos\left(\frac{\mathbf{S_1} \cdot \mathbf{S_2}}{\|\mathbf{S_1}\|\|\mathbf{S_2}\|}\right) \tag{8.6}$$

If both $\mathbf{S_1}$ and $\mathbf{S_2}$ are unit vectors, it can be shown that $ED = 2\sin(\frac{\text{SAM}}{2})$. When SAM is small, $2\sin(\frac{\text{SAM}}{2}) \approx SAM$. It is also worth noting that SAM = arccos(GFC). [54]

Because of this simple relationship between SAM and GFC, we can use the GFC limits found by Romero et al. [53] to formulate acceptable limits for the SAM metric too. The corresponding limits for GFC and SAM are shown in table 8.1.

Table 8.1: Corresponding GFC and SAM quality limits.

Limit	GFC	SAM
Accurate	0.995	0.100
Very good	0.999	0.0447
Excellent	0.9999	0.01414

8.2 Results

For each the calibration phase the measurements were repeated 10 times to statistically analyze the uncertainty of the calibration, with the only exception being the pedestal level measurement. The pedestal level measurements were repeated 20 times, due to the weak nature and low signal-to-noise ratio of the pedestal signal.

All the uncertainties in this section are reported as the standard error of mean (SEM) multiplied with the coverage factor $k = 2$ to make the uncertainty correspond to a 95% confidence interval, as recommended by the Joint Committee for Guides in Metrology (JCGM) [55]. SEM is estimated from the standard deviation and number of the instrument measurements, as shown in equation 8.7.

$$\text{SEM} = \frac{\sigma}{\sqrt{N}} \tag{8.7}$$

Uncertainty is then propagated to the calibration data with the assumption that the noise present in each instrumental measurement is not correlated with the other instruments. [55]

8.2.1 Pedestal level

Pedestal signal of the USB2000+ instrument was measured by repeatedly capturing data in total darkness. The shutter of the programmable light source was closed to prevent any light from entering the integrating sphere.

The pedestal signal of the device under calibration is always a very weak signal, and the signal-to-noise ratio is poor. To minimize uncertainty of the pedestal level, the pedestal measurements are repeated several times. Figure 8.1 shows the decline of the pedestal uncertainty as a function of measurement times.

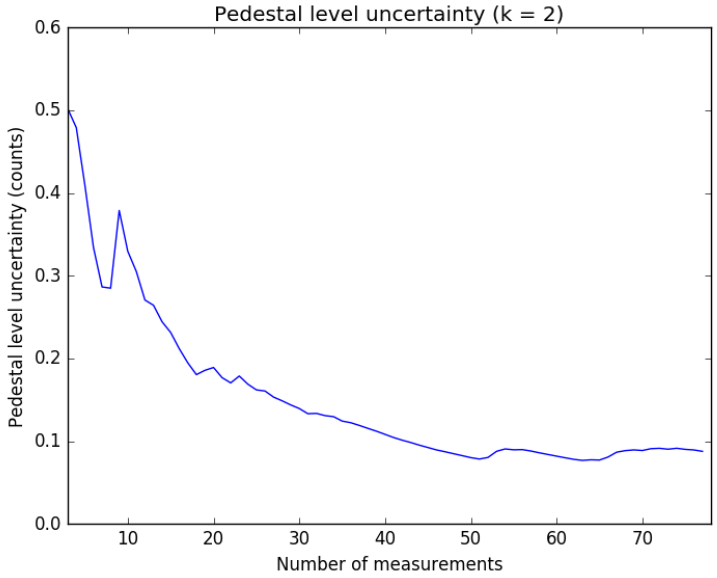

Figure 8.1: USB2000+ pedestal level uncertainty as a function of the number of measurements.

Uncertainty stops declining significantly after 40-50 measurements. For this calibration study 20 repetitions were used as a compromise between uncertainty and total measurement time. Even with 20 repetitions the uncertainty is very small.

Figure 8.2 shows the average pedestal level of the USB2000+ instrument with various integration times. Pedestal correction is done before any of the

other calibration phases, so the pedestal is measured in device-dependent raw counts coming from the spectrometer sensor. For short integration times the pedestal level stays fairly constant over all wavelengths, and thus easy to correct. A significant static pattern starts to arise when integration times reach 1000 milliseconds or more.

USB2000+ features a built-in pedestal correction, which subtracts a constant value from the output signal. The correction still leaves the static error pattern at long integration times. The constant correction value is based on pedestal level measurements a few shielded pixels on the edge of the sensor. Some residual pedestal signal is still left after internal pedestal correction. The error for a single wavelength is very small. However, many color-related operations—such as calculating tristimulus values of the spectrum — involve summing over all the measured spectrum samples, causing any small systematic errors to accumulate and become significant.

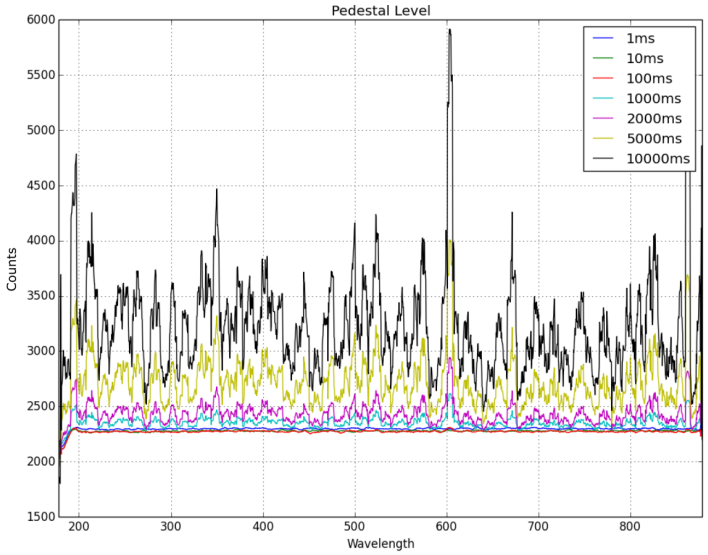

Figure 8.2: Ocean Optics USB2000+ pedestal level as a function of integration time and wavelength.

The device under calibration has no temperature regulation, so the pedestal is very difficult to model accurately. To counter this during characterization, the pedestal level is repeatedly measured right before each actual measurement. This gives us a fairly accurate pedestal model to use.

Temporal stability of the pedestal level was examined by repeating 100

millisecond measurements over a two-minute period right after switching on the device. Repeated measurements heat up the sensor, and may cause changes in the pedestal level. Any large and rapid changes in the pedestal level can cause incorrect pedestal correction, when the pedestal level is measured right before any characterization measurements. Figure 8.3 shows the average pedestal level of all the sensor pixels over time.

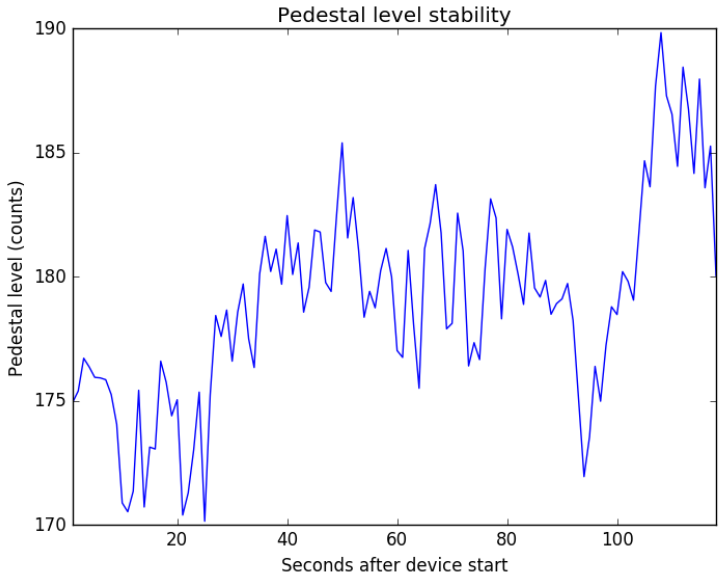

Figure 8.3: Average pedestal level as a function of time for the USB2000+. Measurements were started right after the device was switched on.

As can be seen from the graph, the mean pedestal level varies only slightly, and over long time periods. Since the pedestal level is always measured and compensated for right before any actual measurements, slow changes in the pedestal will not affect the end result.

8.2.2 Linearity calibration

As explained in section 7.3, the USB2000+ has a built-in non-linearity correction (NLC) mechanism, which is based on a 7th degree correction polynomial. For linearity calibration the spectral power distribution of the light source is not important, as long as at least some of the sensor pixels can get saturated with reasonable integration times. The pure xenon spectrum from the programmable light source was used for this study. The non-linearity is

assumed to be identical for all pixels.

An integration time sweep from from 10 milliseconds to 150 milliseconds was run with 10 millisecond increments. Only the sensor pixels that were saturated during the sweep were examined. Dividing the digital values from the sensor with the corresponding integration times gives us the relative sensor response for each pixel and intensity level.

The absolute values of the sensor response divided by the integration time depend on the intensity of the light source at each wavelength. To counter this, a temporary polynomial is fitted to the response data for each pixel, and the data is normalized so that the maximum value of the temporary polynomial is always one. The maximum value of the polynomial is used instead of the maximum value of the data itself to reduce the effect of noise. Figure 8.4 shows the response data for three individual pixels, and the temporary polynomials used to normalize the data.

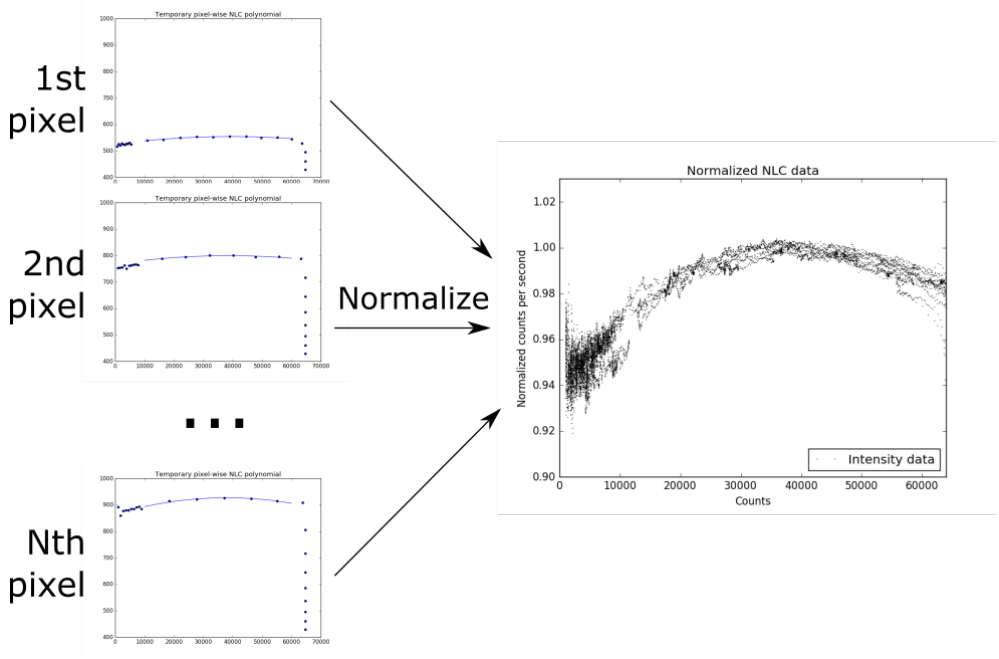

Figure 8.4: Illustration of how the response for each sensor pixel is normalized before fitting the final NLC polynomial.

This operation is done for every pixel that reaches saturation during the integration time sweep, which gives us a big set of data points to use for fitting the final non-linearity correction polynomial, as shown in 8.5.

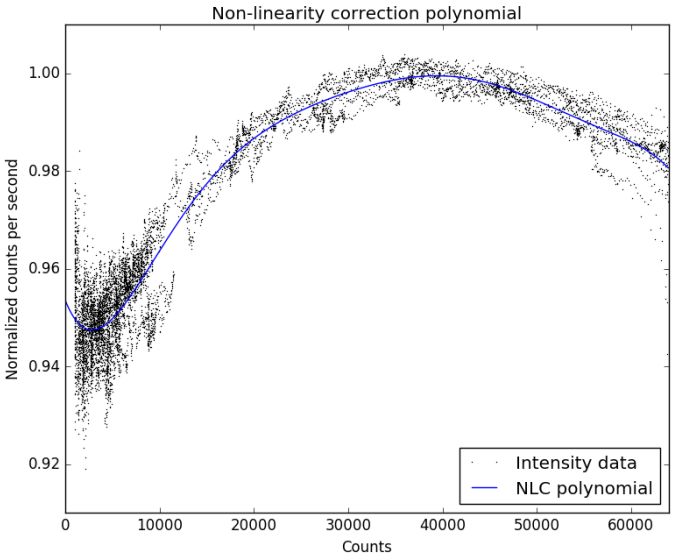

Figure 8.5: Non-linearity correction polynomial fit to integration time sweep data for the USB2000+.

8.2.3 Wavelength calibration

As described in section 7.4, the wavelength calibration of the USB2000+ was determined by producing a comb-like spectrum with the programmable light source, and measuring it with both the USB2000+ and the referenced device PR-650. A 3rd degree polynomial was then formed to match the wavelength samples of USB2000+ to the reference device, as shown in figure 8.6(a). The resulting coefficients are shown in table 8.2.

Table 8.2: Wavelength calibration coefficients.

Coefficient	Coefficient value
I	178.176530
C_1	0.379501970
C_2	-1.47216943e-05
C_3	-2.09760404e-09

Wavelength differences between the calibrated peak locations and the known peak locations are called wavelength calibration residuals, and are

shown in figure 8.6(b). The maximum mean residual is 0.18 nanometers, which is negligible for most purposes, assuming the wavelength calibration of the reference device is correct.

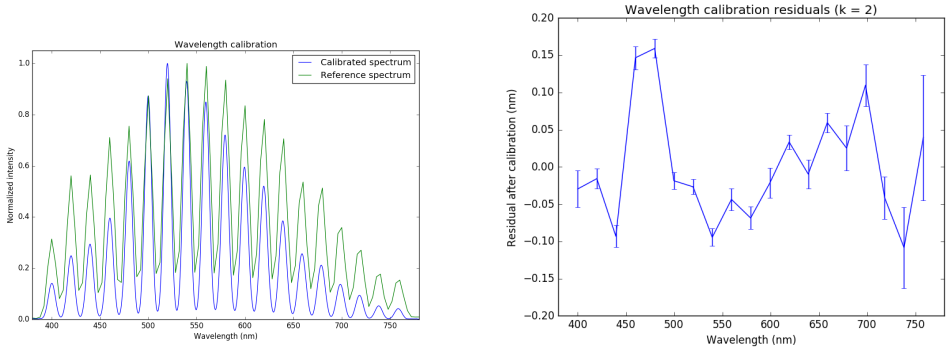

(a) Output after wavelength calibration.

(b) Wavelength calibration residuals.

Figure 8.6: Wavelength calibration results visualized.

8.2.4 Spectral intensity calibration

The spectral calibration procedure described in section 7.5 yields the calibration coefficients shown in figure 8.7(a). The device under calibration and the reference device were shown the full power ouput of the programmable light source to maximize signal-to-noise ratio for the measurements.

Figure 8.7(b) shows the relative uncertainty of the spectral intensity calibration coefficients. The pedestal level of the device under calibration was estimated by averaging 10 measurements right before the actual calibration, and subtracted from the subsequent data. The spectrum was then captured 10 times with both the reference device and the device under calibration. The separate measurements from the reference device were averaged to be used as the reference spectrum for calibration.

Uncertainty of the intensity calibration is at its highest below 400 nanometers and above 700 nanometers, but the uncertainty is still at negligible levels—less than 0.4 percent at maximum. The higher uncertainty below 400 nanometers and above 700 nanometers is most likely due to very low signal of the calibration light source in those wavelength areas.

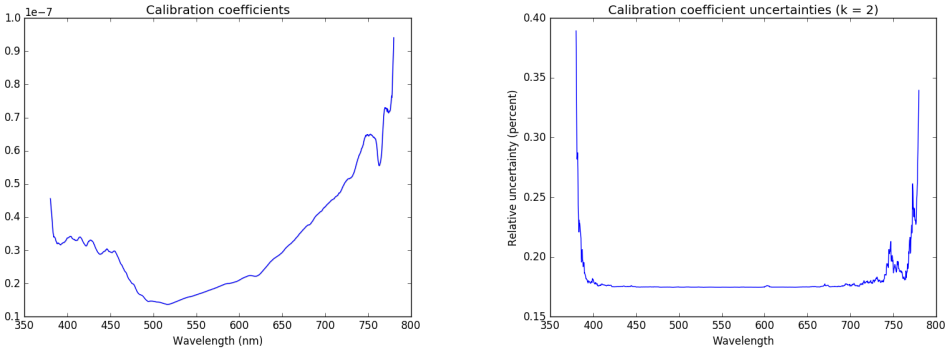

(a) Intensity calibration coefficients.

(b) Intensity calibration uncertainty.

Figure 8.7: Visualization of the spectral intensity calibration data.

8.3 Accuracy in actual use cases

In normal usage the characterization system synthesizes common lighting conditions and standard illuminants into the integrating sphere, and then an image of the inside of the sphere is captured with the camera under characterization. These images are used to provide information for the shading correction and automatic white balance algorithms of the camera image processor.

To evaluate the final performance of the characterization system calibration, multiple CIE standard illuminants [56, 57] were synthesized with the programmable light source, and measured both with the newly calibrated device and the reference device. Names, types and correlated color temperatures (CCT) of the verification illuminants are listed in table 8.3.

CCT is defined as the temperature of the black body radiator whose perceived color most closely resembles that of a given stimulus at the same brightness and under specified viewing conditions [58]. Illuminants with low CCT are perceived as orange-reddish, while higher CCT illuminants are more blue.

The same spectra are very commonly used in the camera characterization and verification process. Illuminants A, F11 and F12 represent common indoor lighting conditions, and D50 and D65 common outdoor lighting conditions. Measurements of the verification illuminants with both the USB2000+ and PR-650 are shown in figure 8.8.

Differences between the reference spectra and the spectra acquired from the device under calibration were calculated using the metrics introduced in section 8.1. The results are shown in figure 8.9. The results are also available

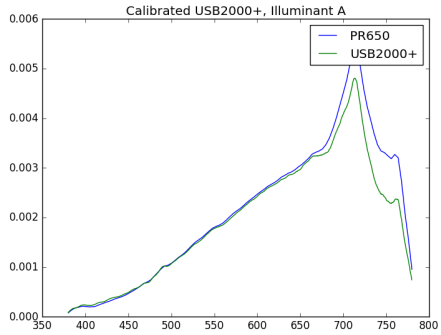

(a) Incandescent illuminant A

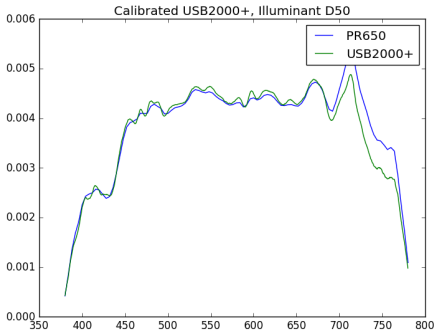

(b) Daylight illuminant D50

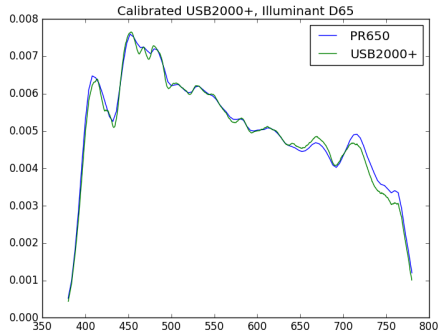

(c) Daylight illuminant D65

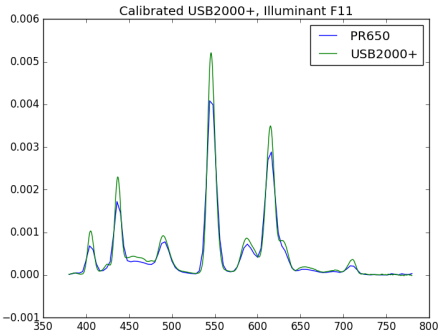

(d) Fluorescent illuminant F11

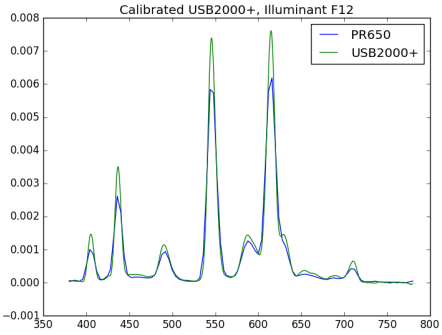

(e) Fluorescent illuminant F12

Figure 8.8: Calibrated USB2000+ spectral radiance output compared to the reference device PR-650 under various illuminants. Output units are in spectral radiance ($W\,m^{-2}\,sr^{-1}\,nm^{-1}$).

Table 8.3: Illuminants used for calibration verification.

Name	Type	CCT
A	Incandescent	2856 K
D50	Horizon light	5003 K
D65	Daylight	6504 K
F11	Fluorescent	4000 K
F12	Fluorescent	3000 K

in numerical form in appendix A. Smaller values indicate a better match for all metrics except GFC. The closer the GFC values get to 1, the better.

To better evaluate the calibration quality for camera characterization, we can ignore any spectral differences at wavelengths above 700 nanometers, since the infrared cutoff filters on camera sensors block any light at such wavelengths from reaching the sensor. For most mobile camera sensors the cutoff point is in the region of 660–680 nanometers, so 700 nanometers is a safe choice. The spectral match results with wavelengths of over 700 nanometers ignored are shown in figure 8.10.

As can be seen in figure 8.8, illuminants A and D50 show considerable error at wavelengths above 700 nm. The error is much smaller for D65 and non-existent for the fluorescent illuminants. Fluorescent illluminants have very little signal over 700 nanometers, which might explain the absence of error. One possible reason for the error could be stray light problems in either the reference device or the device under calibration. Determining the root cause for this requires further study. However, as mentioned above, any error at wavelengths above 700 nm is inconsequential, since the cameras characterized with the system are not sensitive to those wavelengths.

When limiting the examined wavelengths to 700 nanometers, GFC and SAM results for illuminants A, D50 and D65 are very good, considering the limits described in section 8.1. Average GFC of the illuminants A, D50 and D65 is 0.9997.

Results for the fluorescent illuminants are worse, but are still very close to being colorimetrically accurate, with an average GFC of 0.9901. As can be seen in figure 8.8, most of the error comes from the sharp peaks in the spectra. The device under calibration shows higher peaks than the reference device. The reference spectra are sampled relatively sparsely—only at 4 nm intervals. This sparse sampling means that the height of narrow spectral peaks might be underestimated by the reference device, so in this case the spectral difference metrics might overestimate the error with fluorescent illuminants.

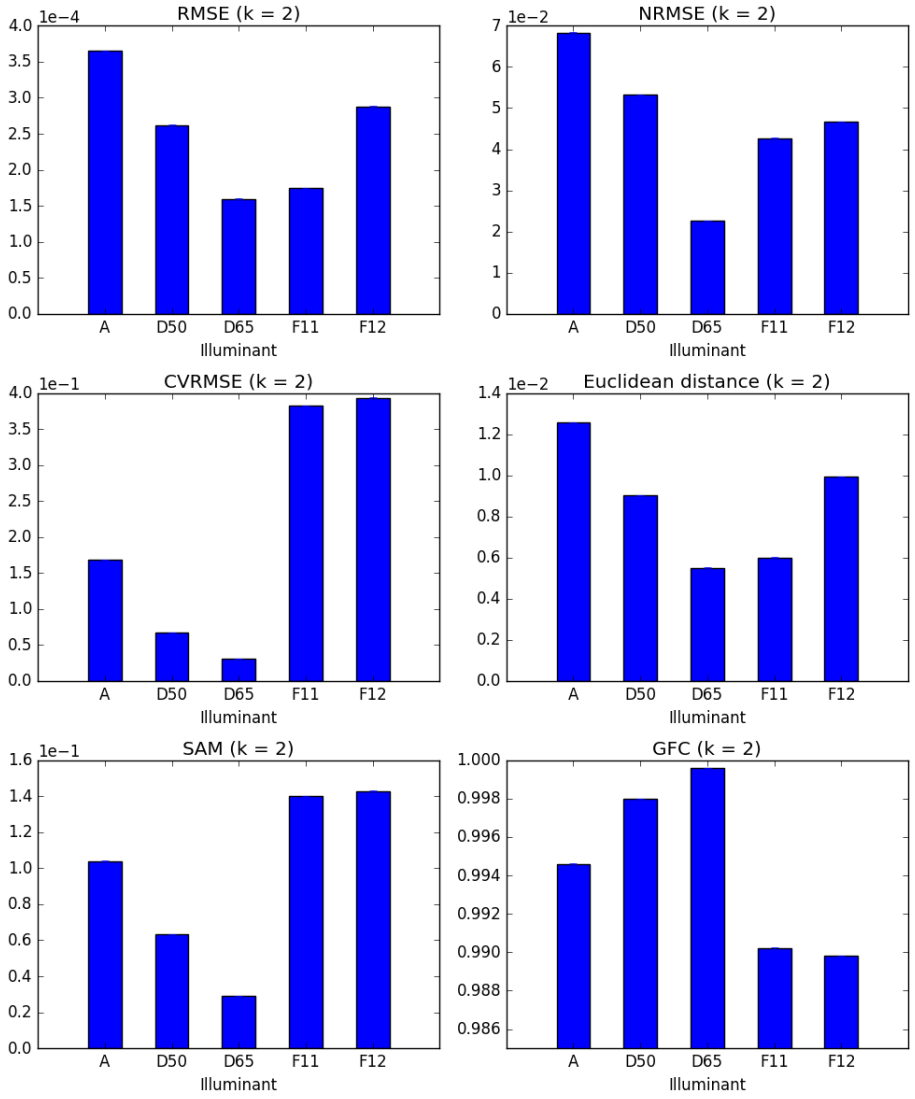

Figure 8.9: Match between the calibrated USB2000+ spectra and the reference spectra measured with the PR-650. Smaller values are better for all metrics except GFC. GFC values close to 1 indicate a good match.

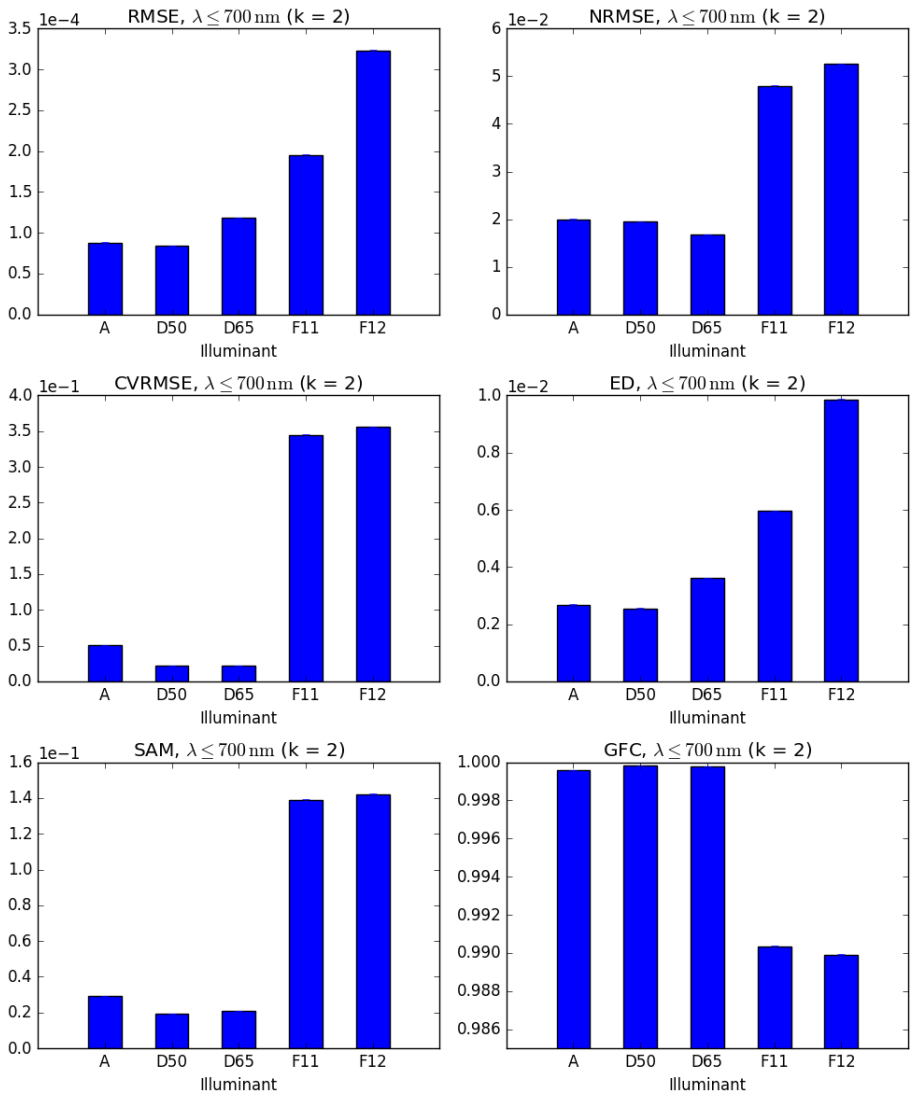

Figure 8.10: Match between the calibrated USB2000+ spectra and the reference spectra measured with the PR-650, when spectral differences at wavelengths above 700 nanometers are ignored. Smaller values are better for all metrics except GFC. GFC values close to 1 indicate a good match.

RMSE-based metrics and ED mostly agree with GFC and SAM. As mentioned in section 8.1, plain RMSE and ED are sensitive to differences in the absolute values of the spectra under comparison. This can be seen by comparing the results for F11 and F12, and to some extent D50 and D65. Maximum radiance values of the F12 spectra used for verification are larger than the maximum values of F11, giving larger values for RMSE and ED. The other metrics and visual comparison show roughly equal calibration quality for both illuminants. Based on this, the normalized variants of RMSE—CV_{RMSE} and NRMSE—seem better suited for comparison of spectra than plain RMSE.

Chapter 9

Conclusions and discussion

In this Master's Thesis the camera characterization system used by Nokia Corporation—and later on by Microsoft—was documented and calibrated, and the calibration process was automated and improved. This was done in such a way that it would interrupt the production use of the system as little as possible.

The calibration calculations and the devices used for calibration were integrated into the company's Mobile Imaging Playground (MIP) software platform, with each calibration phase as its own playground. The MIP components created during the practical work behind this thesis are very modular, and can easily be reused to — for example—accommodate new devices into the calibration system, or analyze existing measurement data instead of data coming directly from the devices.

Multiple metrics were explored for the purpose of evaluating the match between the newly calibrated USB2000+ and the reference device PR-650. GFC and SAM proved to be the most useful metrics, since Romero et al. [53] provided predetermined quality limits for the GFC metric. GFC and SAM are closely related, so the same limits were easily derived for SAM also. ED and the RMSE-based metrics agree with GFC and SAM results.

Uncertainties in the different phases of the calibration process were also evaluated. Measurements were repeated multiple times, making the total uncertainty of the final calibration negligible. The single biggest limiting factor is the calibration uncertainty of the reference device.

For incandescent and daylight illuminants the GFC and SAM results are very good, even bordering on excellent. Narrow peaks in the spectral power distributions of the fluorescent illuminants F11 and F12 are not perfectly reproduced. However, as concluded in section 8.3, the used metrics might overestimate the error for fluorescent spectra, so even they can still be considered at least colorimetrically accurate.

This thesis shows that running the calibration process without disassembling the characterization system is feasible, and it is also feasible without compromising calibration quality. It is now possible to run the calibration process more often than before, and even analyze temporal changes in the calibration. With the new calibration system, it is no longer necessary to send measurement instruments to the manufacturer or a third party for costly calibration. The calibration results still require expert evaluation, but automation of the measurement process frees a lot of time for the system operators to do more productive work, and they can be sure that the system is generating correct results.

Based on the results and observations done during this thesis, some future improvements for the calibration process are proposed below.

In addition to fluorescent light sources, many other modern light sources, such as LEDs, have narrow peaks in their spectra. The current reference spectrometer used in this thesis—PR-650—samples spectra sparsely, only at 4 nanometer intervals. This leaves any narrow peaks in the spectrum undersampled. In the future using a more densely sampling reference device would be helpful in improving resolution of the spectral peaks and other high frequency features.

The implementation and effects of bandpass correction for the spectrometer [44–46] were not investigated in this thesis. Bandpass correction could possibly be useful in handling narrow peaks in the spectra better, and is worth looking into in the future.

Effects of stray light in either the reference device or the device under calibration were not studied in this thesis. After calibration there was some error with illuminants A and D50 at wavelengths above 700 nanometers, and one possible cause for this is stray light in one of the devices.

Quality of the characterization system calibration could also be further evaluated by studying the effects of different calibration errors on the final image quality of a characterized camera module. Modern image processing pipelines are very complex, so it might be difficult to interpret results, but it could be an interesting exercise.

In summary, this study was very interesting, and improved understanding of the instrument calibration process considerably in the Nokia/Microsoft camera image quality organization. Goals of the research were met, and reliability of future measurements was significantly improved by documenting the calibration process and doing uncertainty analysis.

Bibliography

[1] E. Reinhard, E. A. Khan, A. O. Akyüz, and G. M. Johnson, *Color Imaging - Fundamentals And Applications*. Wellesley, Massachusetts: A K Peters, Ltd., 2008.

[2] E. Allen and S. Triantaphillidou, *The Manual of Photography*. Burlington, Massachusetts: Focal Press, 2011.

[3] G. Sharma and R. Bala, *Digital color imaging handbook*. Boca Raton, Florida: CRC Press, 2002.

[4] G. Wyszecki and W. Stiles, *Color Science: Concepts and Methods, Quantitative Data and Formulae*. Hoboken, New Jersey: Wiley-Interscience, 2000.

[5] A. Stockman and L. T. Sharpe, "The spectral sensitivities of the middle- and long-wavelength-sensitive cones derived from measurements in observers of known genotype," *Vision Research*, vol. 40, no. 13, pp. 1711–1737, 2000.

[6] W. D. Wright, "A re-determination of the trichromatic coefficients of the spectral colours," *Transactions of the Optical Society*, vol. 30, no. 4, p. 141, 1929.

[7] J. Guild, "The Colorimetric Properties of the Spectrum," *Philosophical Transactions of the Royal Society of London A: Mathematical, Physical and Engineering Sciences*, vol. 230, no. 681-693, pp. 149–187, 1932.

[8] J. Nakamura, *Image sensors and signal processing for digital still cameras*. Boca Raton, Florida: CRC Press, 2006.

[9] "MOS Capacitor illustration by Cyril Buttay," 2006, accessed April 7th 2016. [Online]. Available: https://commons.wikimedia.org/wiki/File:Mos_capacitance.svg

[10] J. Janesick, *Scientific charge-coupled devices.* Bellingham, Washington: SPIE Publications, 2001.

[11] "QSI High-Resolution Press Photos," 2013, accessed April 7th 2016. [Online]. Available: http://www.qsimaging.com/500photos-hires.html

[12] "Dichroic prism illustration by Colin M.L. Burnett," 2007, accessed April 7th 2016. [Online]. Available: https://commons.wikimedia.org/wiki/File:Dichroic-prism.svg

[13] B. Bayer, "Color imaging array," *US Patent 3,971,065*, 1976.

[14] "Bayer Pattern illustration by Colin M.L. Burnett," 2006, accessed April 7th 2016. [Online]. Available: https://en.wikipedia.org/wiki/File:Bayer_pattern_on_sensor.svg

[15] M. Aghagolzadeh, A. Abdolhosseini Moghadam, M. Kumar, and H. Radha, "Bayer and panchromatic color filter array demosaicing by sparse recovery," in *Proceedings of SPIE*, no. 7876, 2011.

[16] M. Rafinazari and E. Dubois, "Demosaicking algorithm for the Fujifilm X-Trans color filter array," in *2014 IEEE International Conference on Image Processing (ICIP)*, 2014, pp. 660–663.

[17] P. M. Hubel, "Foveon Technology and the Changing Landscape of Digital Cameras," in *Color and Imaging Conference, 13th Color and Imaging Conference Final Program and Proceedings*, 2005, pp. 314–317.

[18] I3A, "CPIQ Initiative Phase 1 White Paper: Fundamentals and review of considered test methods," White Paper, 2007.

[19] A. Getman, T. Uvarov, and Y. Han, "Crosstalk, color tint and shading correction for small pixel size image sensor," Technical Report, 2007, accessed October 31st 2013.

[20] K. Hirakawa, "Cross-talk explained," in *2008 15th IEEE International Conference on Image Processing*, 2008, pp. 677–680.

[21] X. Wu and X. Zhang, "Joint color decrosstalk and demosaicking for CFA cameras." *IEEE transactions on image processing : a publication of the IEEE Signal Processing Society*, vol. 19, no. 12, pp. 3181–3189, 2010.

[22] V. Nummela, J. Viinikanoja, and J. Alakarhu, "Cameras in mobile phones," in *Proceedings of SPIE*, vol. 6196, 2006, p. 61960B.

[23] J. F. James, *Spectrograph Design Fundamentals.* Cambridge: Cambridge University Press, 2007.

[24] N. V. Tkachenko, *Optical Spectroscopy: Methods and Instrumentations*, 1st ed. Oxford: Elsevier, 2006.

[25] G. Hong, M. R. Luo, and P. A. Rhodes, "A study of digital camera colorimetric characterisation based on polynomial modelling," *Color Research and Application*, vol. 26, no. 1, pp. 76–84, 2001.

[26] "Gretag-Macbeth ColorChecker photograph by Richard F. Lyon," 2000, accessed April 7th 2016. [Online]. Available: https://en.wikipedia.org/wiki/File:Gretag-Macbeth_ColorChecker.jpg

[27] R. Berry and J. Burnell, *The Handbook of Astronomical Image Processing*, 2nd ed. Richmond, Virginia: Willmann-Bell Inc., 2005.

[28] Y. Bérube, D. Gingras, and F. P. Ferrie, "Color Camera Characterization with an Application to Detection under Daylight," in *Vision Interface*, 1999, pp. 280–287.

[29] P. L. Vora, J. E. Farrell, J. D. Tietz, and D. H. Brainard, "Linear Models for Digital Cameras," in *Proceedings of the IS&T's 50th Annual Conference*, 1997, pp. 377–382.

[30] "OL 490 Agile Light Source," accessed April 7th 2016. [Online]. Available: http://www.ghinstruments.com/products/spectral-imaging-synthesis/ol490-agile-light-source/

[31] W. Fateley, "Radiation filter, spectrometer and imager using a micromirror array," *US Patent 6,128,078*, 2000.

[32] D. Dudley, W. Duncan, and J. Slaughter, "Emerging Digital Micromirror Device (DMD) Applications," in *Proceedings of SPIE*, vol. 4985, 2003, pp. 14–25.

[33] "USB2000+ Miniature Fiber Optic Spectrometer," accessed October 31st 2013. [Online]. Available: http://www.oceanoptics.com/products/usb2000+.asp

[34] "Photo Research, Inc. - PR-650 SpectraScan Colorimeter," accessed October 25th 2013. [Online]. Available: http://www.photoresearch.com/current/pr650.asp

[35] "Gigahertz-Optik - Light - Measurement - System Components," accessed November 4th 2013. [Online]. Available: http://www.gigahertz-optik.de/15-1-Light+-+Measurement+-+System+Components.html

[36] "Scooby2 Platform - Atra Vision Inc." accessed 29th November 2013. [Online]. Available: http://www.atravision.com/scooby/scooby2.php

[37] "SMIA 1.0, Part 1, Functional Specification," Nokia & STMicroelectronics, Standard, 2004.

[38] "MIPI Alliance," 2015, accessed April 7th 2016. [Online]. Available: http://mipi.org/

[39] J. J. C. Zwinkels, "Colour-measuring instruments and their calibration," *Displays*, vol. 16, no. 4, pp. 163–171, 1996.

[40] Photo Research Inc., "Spectrometer Certificate of Compliance and Conformance," Calibration Certificate, 2014.

[41] "USB2000+ Fiber Optic Spectrometer - Installation and Operation Manual," accessed November 11th 2014. [Online]. Available: http://oceanoptics.com/wp-content/uploads/USB2000-Operating-Instructions1.pdf

[42] "OL 700-24 Wavelength Calibration Source," accessed March 7th 2014. [Online]. Available: http://www.liberohk.com/images/Optronic_Laboratories/PDF/1250185582B164_700-24_8-09.pdf

[43] S. Kallio, "Improving optical measurement accuracy of small LCD panels by using advanced calibration process and uncertainty analysis," Master's Thesis, Helsinki University of Technology, 2006.

[44] S. Eichstädt, F. Schmähling, G. Wübbeler, U. Krüger, and C. Elster, "A new approach to bandpass correction in spectrometer measurements using the Richardson-Lucy method," in *The 16th International Congress of Metrology*, vol. 14005, 2013, pp. 1–5.

[45] S. Eichstädt, F. Schmähling, G. Wübbeler, K. Anhalt, L. Bünger, U. Krüger, and C. Elster, "Comparison of the Richardson–Lucy method and a classical approach for spectrometer bandpass correction," *Metrologia*, vol. 50, no. 2, p. 107, 2013.

[46] E. R. Woolliams, R. Baribeau, A. Bialek, and M. G. Cox, "Spectrometer bandwidth correction for generalized bandpass functions," *Metrologia*, vol. 48, no. 3, p. 164, 2011.

[47] ".NET Downloads, Developer Resources & Case Studies — Microsoft .NET Framework," accessed November 4th 2013. [Online]. Available: http://www.microsoft.com/net

[48] "ISO/IEC 23270:2003 - C# Language Specification," ISO/IEC, Standard, 2003.

[49] "NI LabVIEW - Improving the Productivity of Engineers and Scientists - National Instruments," accessed March 7th 2014. [Online]. Available: http://www.ni.com/labview/

[50] "Simulink - Simulation and Model-Based Design - MathWorks Nordic," accessed March 7th 2014. [Online]. Available: http://www.mathworks.se/products/simulink/

[51] F. Imai, M. Rosen, and R. S. Berns, "Comparative Study of Metrics for Spectral Match Quality," in *CGIV 2002: The First European Conference on Colour Graphics, Imaging, and Vision*, 2002, pp. 492–496.

[52] "FAQ: What is the coefficient of variation?" accessed March 21st 2016. [Online]. Available: http://www.ats.ucla.edu/stat/mult_pkg/faq/general/coefficient_of_variation.htm

[53] J. Romero, A. García-Beltrán, and J. Hernández-Andrés, "Linear bases for representation of natural and artificial illuminants," *Journal of the Optical Society of America A*, vol. 14, no. 5, pp. 1007–1014, 1997.

[54] C.-I. Chang, "An information-theoretic approach to spectral variability, similarity, and discrimination for hyperspectral image analysis," *IEEE Transactions on Information Theory*, vol. 46, no. 5, pp. 1927–1932, 2000.

[55] Joint Committee for Guides in Metrology (JCGM), *Evaluation of measurement data: Guide to the expression of uncertainty in measurement*. Geneva: ISO, 2008.

[56] "CIE 15:2004 - Colorimetry, 3rd Edition," CIE, Technical Report, 2004.

[57] "ISO 11664-2:2007(E)/CIE S 014-2/E:2006 - CIE Colorimetry - Part 2: Standard Illuminants for Colorimetry," CIE/ISO, Standard, 2007.

[58] "CIE 17.4-1987 - International Lighting Vocabulary, 4th Edition," CIE, Technical Report, 1987.

Appendix A

Spectral match results

A.1 Wavelengths 380–780 nm

The metrics in this section are calculated based on the whole 380–780 nm range of the reference device PR-650.

Table A.1: RMSE between the calibrated USB2000+ spectra and the reference spectra measured with the PR-650.

Illuminant	RMSE	Uncertainty (k = 2)
A	0.0003649995669906682	4.004507546430755e-07
D50	0.00026100119525957513	5.974443239630429e-07
D65	0.00015983781961025463	4.199425979341055e-07
F11	0.00017404158138439337	5.239526540546178e-07
F12	0.0002879261714602532	7.930894595131497e-07

Table A.2: NRMSE between the calibrated USB2000+ spectra and the reference spectra measured with the PR-650.

Illuminant	NRMSE	Uncertainty (k = 2)
A	0.06835275764052232	7.49916324689282e-05
D50	0.05295919746370124	0.00012122615720153653
D65	0.022637465949821155	5.94755126464627e-05
F11	0.042647159195482086	0.00012838938873469896
F12	0.04661499841385323	0.00012840049832827608

Table A.3: CVRMSE between the calibrated USB2000+ spectra and the reference spectra measured with the PR-650.

Illuminant	CVRMSE	Uncertainty (k = 2)
A	0.16831506607774366	0.00018466294572441346
D50	0.0672742290288261	0.00015399395486403287
D65	0.03149243264995155	8.274020513125753e-05
F11	0.3819655702960122	0.0011499083881113684
F12	0.393073661479569	0.0010827170595526102

Table A.4: Euclidean distance (ED) between the calibrated USB2000+ spectra and the reference spectra measured with the PR-650.

Illuminant	ED	Uncertainty (k = 2)
A	0.012580577271222883	1.3802486681403354e-05
D50	0.008996026301939603	2.0592338080945616e-05
D65	0.005509190208222915	1.4474319370694401e-05
F11	0.005998756604191168	1.8059273070219747e-05
F12	0.009924059577187644	2.7335712506893717e-05

Table A.5: SAM between the calibrated USB2000+ spectra and the reference spectra measured with the PR-650.

Illuminant	SAM	Uncertainty (k = 2)
A	0.10389518405053622	0.0002252426743494236
D50	0.06298463655782305	0.00015559868389130156
D65	0.0290812550478318	8.28821574834942e-05
F11	0.139809108343465	0.00036961352190916495
F12	0.14285501696403569	0.0003030430324632032

Table A.6: GFC between the calibrated USB2000+ spectra and the reference spectra measured with the PR-650.

Illuminant	GFC	Uncertainty (k = 2)
A	0.9946076853324352	2.3331757338531823e-05
D50	0.9980170932218065	9.794495002490645e-06
D65	0.9995771615201313	2.4168536088318714e-06
F11	0.9902424466863282	5.151945602214414e-05
F12	0.9898134494875167	4.315970926429243e-05

A.2 Wavelengths 380–700 nm

The spectral match calculations in this section have been limited to the wavelength range 300–700 nm to better reflect the calibration quality when the system under calibration is used with cameras that are not sensitive to light with wavelengths above 700 nm.

Table A.7: RMSE between the calibrated USB2000+ spectra and the reference spectra measured with the PR-650, when spectral differences at wavelengths above 700 nanometers are ignored.

Illuminant	RMSE	Uncertainty (k = 2)
A	8.893494879677183e-05	2.623537360476484e-07
D50	8.282762183307551e-05	6.395640166390536e-07
D65	0.00011887623639622034	7.374254647149581e-07
F11	0.00019455906089915764	6.538189922394726e-07
F12	0.00032295452283444156	5.030792904934182e-07

Table A.8: NRMSE between the calibrated USB2000+ spectra and the reference spectra measured with the PR-650, when spectral differences at wavelengths above 700 nanometers are ignored.

Illuminant	NRMSE	Uncertainty (k = 2)
A	0.020203372216487124	5.9598956917025126e-05
D50	0.019285677693754492	0.0001489168132133706
D65	0.016836170314536002	0.00010443988718515368
F11	0.047819957876351064	0.0001606997716948024
F12	0.05259401895173292	8.19278253365695e-05

Table A.9: CVRMSE between the calibrated USB2000+ spectra and the reference spectra measured with the PR-650, when spectral differences at wavelengths above 700 nanometers are ignored.

Illuminant	CVRMSE	Uncertainty (k = 2)
A	0.05079563283265563	0.0001498446249629538
D50	0.021248062669792976	0.00016406961839708956
D65	0.021857012009892436	0.00013558569590774665
F11	0.34313090261670953	0.0011530971619530962
F12	0.3558397246905383	0.0005543058962467573

Table A.10: Euclidean distance (ED) between the calibrated USB2000+ spectra and the reference spectra measured with the PR-650, when spectral differences at wavelengths above 700 nanometers are ignored.

Illuminant	ED	Uncertainty (k = 2)
A	0.002717977751882906	8.017901031576796e-06
D50	0.002531329206677877	1.9545980423310398e-05
D65	0.0036330258253235515	2.2536764611483177e-05
F11	0.005945999925850709	1.998163262820584e-05
F12	0.009869946739833666	1.537481426023817e-05

Table A.11: SAM between the calibrated USB2000+ spectra and the reference spectra measured with the PR-650, when spectral differences at wavelengths above 700 nanometers are ignored.

Illuminant	SAM	Uncertainty (k = 2)
A	0.029539575260656988	0.0002122835911947575
D50	0.019191931820471315	0.00015205755376587805
D65	0.0211696510738698	0.00013721149865503942
F11	0.13881000264935994	0.0003726608179804709 3
F12	0.14241934635186465	0.00024562859910659746

Table A.12: GFC between the calibrated USB2000+ spectra and the reference spectra measured with the PR-650, when spectral differences at wavelengths above 700 nanometers are ignored.

Illuminant	GFC	Uncertainty (k = 2)
A	0.9995636821652066	6.259841671288693e-06
D50	0.9998158116326948	2.925508821424489e-06
D65	0.9997759077765315	2.9046397702031343e-06
F11	0.9903811790596538	5.142609518420193e-05
F12	0.9898754207817311	3.4905665896562004e-05